Check for updates

Photocatalytic and bactericidal properties and molecular docking analysis of TiO$_2$ nanoparticles conjugated with Zr for environmental remediation

M. Ikram, [ID] *[a] J. Hassan,[b] A. Raza,[b] A. Haider,[c] S. Naz,[d] A. Ul-Hamid, [ID] *[e] J. Haider,[d] I. Shahzadi,[f] U. Qamar[b] and S. Ali[b]

Despite implementing several methodologies including a combination of physical, chemical and biological techniques, aquatic and microbial pollution remains a challenge to this day. Recently, nanomaterials have attracted considerable attention due to their extraordinary prospective for utilization toward environmental remediation. Among several probable candidates, TiO$_2$ stands out due to its potential for use in multifaceted applications. One way to improve the catalytic and antimicrobial potential of TiO$_2$ is to dope it with certain elements. In this study, Zr-doped TiO$_2$ was synthesized through a sol–gel chemical method using various dopant concentrations (2, 4, 6, and 8 wt%). Surface morphological, microstructural and elemental analysis was carried out using FESEM and HR-TEM along with EDS to confirm the formation of Zr–TiO$_2$. XRD spectra showed a linear shift of the (101) anatase peak to lower diffraction angles (from 25.4° to 25.08°) with increasing Zr^{4+} concentration. Functional groups were examined *via* FTIR, an ample absorption band appearing between 400 and 700 cm^{-1} in the acquired spectrum was attributed to the vibration modes of the Ti–O–Ti linkage present within TiO$_2$ nanoparticles, which denotes the formation of TiO$_2$. Experimental results indicated that with increasing dopant concentrations, photocatalytic potential was enhanced significantly. In this respect, TiO$_2$ doped with 8 wt% Zr (sample 0.08 : 1) exhibited outstanding performance by realizing 98% elimination of synthetic MB in 100 minutes. This is thought to be due to a decreased rate of electron–hole pair recombination that transpires upon doping. Therefore, it is proposed that Zr-doped TiO$_2$ can be used as an effective photocatalyst material for various environmental and wastewater treatment applications. The good docking scores and binding confirmation of Zr-doped TiO$_2$ suggested doped nanoparticles as a potential inhibitor against selected targets of both *E. coli* and *S. aureus*. Hence, enzyme inhibition studies of Zr-doped TiO$_2$ NPs are suggested for further confirmation of these *in silico* predictions.

1. Introduction

Titanium dioxide (TiO$_2$), is a promising material that is widely used due to its low cost, ease of availability, high stability, non-toxicity, optoelectronic nature, and especially excellent photo-catalytic properties.[1,2] TiO$_2$ exists in numerous crystallographic forms including anatase (tetragonal), rutile (tetragonal), and brookite (orthorhombic); among these anatase is the most

[a]Solar Cell Applications Research Lab, Department of Physics, Government College University Lahore, 54000, Punjab, Pakistan. E-mail: dr.muhammadikram@gcu.edu.pk

[b]Department of Physics, Riphah Institute of Computing and Applied Sciences (RICAS), Riphah International University, 14 Ali Road, Lahore, Pakistan

[c]Department of Clinical Medicine and Surgery, University of Veterinary and Animal Sciences, Lahore 54000, Punjab, Pakistan

[d]Tianjin Institute of Industrial Biotechnology, Chinese Academy of Sciences, Tianjin 300308, China

[e]Center for Engineering Research, Research Institute, King Fahd University of Petroleum & Minerals, Dhahran, 31261, Saudi Arabia. E-mail: anwar@kfupm.edu.sa

[f]College of Pharmacy, University of the Punjab, Lahore, 54000, Pakistan

significant and stable compound. Large surface area, high degree of crystallinity, and superior physical and chemical properties make TiO$_2$ a reliable source for use in biological sensors, medical diagnosis, and solar cell applications.[3,4] TiO$_2$ nanoparticles exhibit highly improved properties when compared with their bulk counterparts solely due to the former's nano-based structure.[5] Anatase TiO$_2$ has a wide band gap ($\sim$3.2 eV) compared to rutile ($\sim$3.02 eV) and can absorb UV light up to 387 nm, which is appropriate for photocatalysis. This wide band gap enables 4% of solar energy present on earth's surface to be utilized.[6,7] Anatase TiO$_2$ semiconductor reveals excellent characteristics due to high absorbance and electron recombination rate compared to rutile.[8] Various methods are used to synthesize TiO$_2$ including thermal evaporation,[9] precipitation,[10] chemical vapor deposition (CVD),[11] hydro-thermal,[12] and mechanical ball milling.[13] Among these, sol–gel technique[14] is attractive due to its ability to attain homogenous, ultrafine nanoparticles with outstanding morphology. Another important advantage of sol–gel process is that it enables

synthesis of materials with required stoichiometry and desired amount of doping with uniform dispersion.[15]

Titania however suffers from a number of drawbacks that limit its practical applications in photocatalysis. Firstly, the photogenerated electrons and holes coexist in titania particle and probability of their recombination is high. This leads to a low rate of desired chemical transformation with respect to the absorbed light energy. The relatively large band gap energy (~3.2 eV) requires ultraviolet light for photoactivation, resulting in a very low efficiency in utilizing solar light. UV light accounts for only about 5% of the solar spectrum compared to visible light (45%).[16,17] In addition, since titania is non-porous with a polar surface, it exhibits low absorption capability for non-polar organic pollutants. Also, the challenge to recover nano-sized titania particles from treated water adds to both economic and safety concerns. The TiO_2 nanoparticles also suffer from aggregation and agglomeration which affect pho-toactivity as well as light absorption. Several strategies have been employed to overcome these drawbacks.[16,18] These strate-gies include extending the wavelength of photoactivation of TiO_2 into visible region of the spectrum thereby increasing the utilization of solar energy; preventing electron/hole pair recombination and thus allowing more charge carriers to successfully diffuse to the surface; increasing the absorption affinity of TiO_2 towards organic pollutants as well as preventing the aggregation and agglomeration of nano-titania particles while easing their recovery from treated water.[16,19,20]

Heavy metal ions found in industrial and livestock waste may precipitate several ailments that can endanger human and acoustic life. Various methods such as sorption, chemical oxidation, and filtration are deployed to purify wastewater.[21–27] Among these, photocatalysis is a remarkable application that can be employed for converting solar energy into chemical energy without any harmful side effects.[23–25,27–30] Various strat-egies are employed to enhance the photocatalytic activity of TiO_2 catalyst that was discovered in 1972 by Honda and Fujishima.[31,32] Metal doping has been extensively used to advance efforts at developing modified TiO_2 photocatalysts to operate efficiently under visible light. The photoactivity of metal-doped TiO_2 photocatalysts depends to a large extent on the nature of the dopant ion, its concentration, the method used for doping, the type of TiO_2 used as well as the reaction for which the catalyst is used and the reaction conditions, and the mechanism of lowering of band gap energy of TiO_2 with metal doping.[16,33,34] It is believed that doping TiO_2 with metals results in an overlap of the Ti 3d orbitals with d levels of metals causing a shift in the absorption spectrum to longer wavelengths which in turn favors the use of visible light to photoactivate TiO_2.[16] A review of the relevant literature in this regard signifies that doping TiO_2 with a transition metal such as Au,[35] Ag,[36] Cr, and Pt[37] is an effective approach to enhance photocatalytic potential of the host material for use in impurity degradation applica-tions. Besides, co-doping with multiple metals serves to increase efficiency and as a result enhance the efficacy of pho-tocatalytic process.[13,38,39] Several studies using various approaches to modify TiO_2 with an aim to improve its photo-catalytic activity have been reported. The most achievable

method thus far appears to be doping with metal or nonmetals. Doping with metallic or nonmetallic ions serves to overcome migration of excitons from the inside of photocatalyst to the surface by suppressing excitons recombination that is gener-ated through employment of light, thus raising photo quantum efficiency.[40,41] Within the TiO_2 structure, recombination of excitons is inhibited through charge trapping when an appro-priate amount of Zr^{+4} ions replaces Ti^{4+} which in turn causes to accelerate photocatalytic activity.[42] Host Ti and dopant Zr both correspond to IV-B group of periodic table and interestingly oxides of these two materials (TiO_2 and ZrO_2) are n-type semi-conductors that exhibit comparable physical and chemical properties. Collective precipitation of Ti and Zr salts causes to compound their mutual interaction.[42] Doping of transition metal in the TiO_2 lattice gives rise to surface modification and crystal defects while altering its photocatalytic activity by sup-pressing excitons recombination through the phenomenon of trapping.[43] Furthermore, Zr belongs to isoelectric impurity element with deep energy level doping.[28,44] Besides this, the presence of Zr provides synergistic effects that further contribute to the improvement in photocatalysis. Interest in Zr-doped TiO_2 nanocomposite is well placed since both Zr and TiO_2 have similar valance structure. Substitutional doping of Zr in TiO_2 serves to enhance bond length, and stabilize anatase phase.[36]

Another emerging application of TiO_2 nanoparticles is as an antibacterial agent. This bactericidal characteristic of TiO_2 is primarily attributed to the oxidative stress present due to the production of reactive oxygen species (ROS) containing hydroxyl radicals *i.e.* OH$^•$ and generation of hydrogen peroxide (H_2O_2) under ultra-visible light, therefore, rendering TiO_2 as a potent means to kill bacteria.[45–47] The generated ROS leads to direct contact between cells and nanoparticles, which cause cell death due to the damage induced in the cell membrane and DNA, ultimately resulting in cessation of cell cycle.[46,48–50] It prevents and destroys major pathogens and foodborne such as *E. coli*, Methicillin-resistant *Staphylococcus aureus* (MRSA), *Bacillus subtilis*, *S. aureus*, and Pseudomonas[24,26,51–53]. Several Zr-based materials show promising biological responses due to their excellent biocompatibility. Both the crystal structure and shape of TiO_2 NPs are the most important factors that affect their physicochemical properties, and therefore their antimicrobial behavior.[54,55] With respect to crystal structure, anatase exhibits the highest photocatalytic and antimicrobial activity. Some works have shown that anatase structure can produce OH$^•$ radicals in a photocatalytic reaction, and as explained above, bacteria wall and membranes are effectively terminated.[55,56] Certainly, in some studies, these materials have also shown high effectiveness at reducing the feasibility of adherent bacterial species such as *E. coli*, Methicillin-resistant *Staphylo-coccus aureus* (MRSA), *Bacillus subtilis*, *S. aureus*, and Pseudo-monas and therefore have been extensively used in biomedical applications.[57–60]

In the current research work, we aimed to synthesize TiO_2 nanoparticles doped with various concentrations (2, 4, 6, and 8 wt%) of Zr through sol–gel method. The synthesized products were employed as photocatalysts to treat industrial wastewater

and remove synthetic dye (Methylene blue). Furthermore, the level of its antimicrobial activity was evaluated against Methicillin-resistant *Staphylococcus aureus* (MRSA). High antibacterial activity of Zr-doped TiO$_2$ against *S. aureus* was attributed to cell wall rupture and/or to other biosynthetic pathways considered vital for bacterial survival and growth. Molecular docking analysis was performed to provide an insight into the interaction pattern of Zr-doped TiO$_2$ nanoparticles with selected protein targets such as dihydrofolate reductase (DHFR) and dihydropteroate synthase (DHPS) of folate biosynthetic pathway along with DNA gyrase from both *E. coli* and *S. aureus*.

2. Experimental section

2.1 Materials

Titanium(IV) butoxide (Ti(OBu)$_4$) (98%), zirconium acetate (C$_4$H$_6$O$_4$Zr) were purchased from Sigma-Aldrich Co. (Germany) and hydrochloric acid (HCl, 37%) was acquired from Analar. Reagents used in this research were employed without additional purification.

2.2 Synthesis of pure and Zr-doped TiO$_2$ samples

Pure TiO$_2$ and Zr-doped TiO$_2$ samples were synthesized using sol–gel method. Initially, 10 ml of Ti(OBu)$_4$ was dissolved in 50 ml methanol and 3 ml deionized water with the addition of 2 ml HCL under stirring for 2 hours; this solution was considered solution 1. Various concentrations of zirconium acetate (2, 4, 6, and 8 wt%) were vigorously dissolved in deionized water referred to as solution 2. Later, solution 2 was added dropwise into solution 1 under constant stirring. During synthesis, a mixture of water and ethanol was added gradually and the solution was magnetically stirred at 50 °C for 2 hours. Finally, prepared products were annealed at 400 °C to acquire nanoparticles of anatase as shown in Fig. 1.[41,61]

2.3 Evaluation of photocatalytic activity

Photocatalytic activity of prepared products was evaluated by recording significant degradation rate of certain industrial pollutants such as synthetic and toxic methylene blue (MB) dye in aqueous solution as displayed in Fig. 2. The stock solution of MB (5 g/500 ml) was arranged and 10 mg of prepared photocatalysts (0 : 1, 0.02 : 1, 0.04 : 1, 0.06 : 1, and 0.08 : 1) were blended with 60 ml stock solution, which was retained in dark

for 30 min to attain equilibrium between MB and photocatalyst before exposing it to light. After strong stirring for 15 min, the solution was transferred to a photoreactor operated with a Hg lamp (400 W with a wavelength of 400–700 nm). A distance of 15 cm was kept between the solution and light source to inhibit overheating. After complete exposure to light for a fixed time interval of 20 minutes, 3 ml of solution was extracted to measure dye concentration using a UV-vis spectrograph at λ_{max} = 665 nm of MB absorbance. The collected solution was centrifuged at 4000 rpm for 5 minutes to extract photocatalyst from the solution to check the reusability of samples. Dye absorbance decreased gradually at λ_{max} after fixed time intervals that demonstrated decolorization rate and PCA efficiency of photocatalysts as calculated using eqn (1).

$$\text{Degradation efficiency (\%)} = \left(\frac{C_o - C}{C_o}\right) \times 100 \qquad (1)$$

where C_o corresponds to initial absorbance (*i.e.* $t = 0$) and C refers to final absorbance at time t.[27,62,63]

2.3.1 Reaction mechanism and kinetics. A measure of reactions to control degradation of organic molecules through photocatalytic experiments can be described as follows (see Fig. 2):

I. Photoexcitation. The photocatalytic reaction is prompted by photons of energy $E = h\nu$ or those with energy higher than the band gap energy, such that photoelectrons (e$^-$) are shifted from the lower band (valance band-VB) to higher band (conduction band-CB). The excitation process generates a hole in VB thus resulting in one electron–hole pair (e$^-$–h$^+$) as depicted in eqn 2

$$\text{TiO}_2 + h\nu \rightarrow \text{TiO}_2(\text{e}^-) + \text{h}^+ \qquad (2)$$
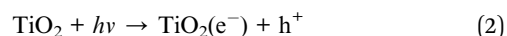
II. Ionization of water. Photogenerated h$^+$ produce OH$^•$ free radical after reaction with water:

$$\text{H}_2\text{O(ads)} + \text{h}^+ \rightarrow \text{OH}^•\text{(ads)} + \text{H}^+\text{(ads)} \qquad (3)$$
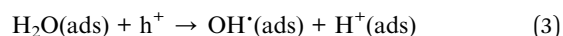
The HO$^•$ radical produced on the irradiated surface of semiconductor is a strong oxidant agent. It selectively targets adsorbed organic molecules or those which are very close to the catalyst surface that contributes to mineralization depending on the structure and degree of stability. In this manner,
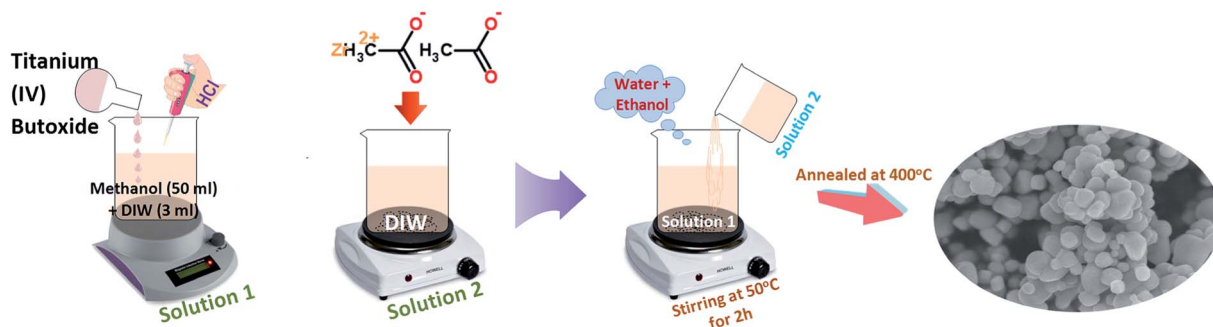

Fig. 1 Synthesis process for TiO$_2$ and Zr-doped TiO$_2$ nanoparticles.

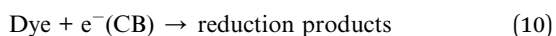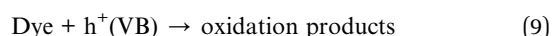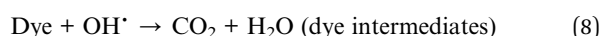biological compounds are attacked easily and microorganisms are eliminated to enhance decontamination.
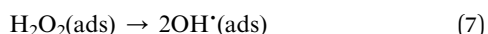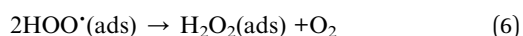
Not only it can quickly target biological compounds, but microorganisms can be killed to enhance decontamination.

III. Oxygen ionosorption. Photogenerated electrons are readily picked up by oxygen molecules to produce superoxide radicals (O_2^-) and electrons interacting with surface-bound water molecules (OH^-).

$$O_2 + e^- \rightarrow O_2^{\bullet-} (ads) \tag{4}$$
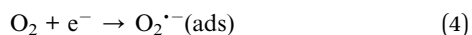
The superoxide ion can not only take part in more oxidation cycles, but it can also inhibit recombination of $e^- $–$h^+$ and thus serves to keep TiO_2 molecule neutral.

IV. Protonation of superoxide. Superoxide ions (O_2^-) provide protonated hydroperoxylate radical ($H_2O^{\bullet}$) and finally H_2O_2 is dissociated into strongly reactive $OH^{\bullet}$.

$$O_2^{\bullet-}(ads) + H + \rightleftharpoons HOO^{\bullet}(ads) \tag{5}$$

$$2HOO^{\bullet}(ads) \rightarrow H_2O_2(ads) + O_2 \tag{6}$$

$$H_2O_2(ads) \rightarrow 2OH^{\bullet}(ads) \tag{7}$$

$$Dye + OH^{\bullet} \rightarrow CO_2 + H_2O \text{ (dye intermediates)} \tag{8}$$

$$Dye + h^+(VB) \rightarrow \text{oxidation products} \tag{9}$$

$$Dye + e^-(CB) \rightarrow \text{reduction products} \tag{10}$$

Oxidation and reduction processes take place simultaneously on the surface of photo-excited photocatalyst.[64–66]

2.4 Isolation and identification of *S. aureus* and *E. coli*

Goat (caprine) clinically positive mastitis milk samples were collected from private farms of Punjab (Pakistan) and cultured on 5% sheep blood agar (SBA). The cultured isolates were further purified by streaking on MacConkey agar (MA) and mannitol salt agar (MSA) in order to isolate *E. coli* and *S. aureus*, respectively in triplets. Morphological and biochemical characterization of purified isolates was undertaken through Gram's staining, catalase, and coagulase tests.[67]

2.5 Antimicrobial activity

Antimicrobial evaluation of Zr-doped TiO_2 was undertaken through agar well diffusion assay by swabbing 1.5×10^8 CFU ml^{-1} of isolated G −ve and G +ve stains on MA and MSA, respectively. Various ratios of Zr-doped TiO_2 (0.5 mg/50 μl) & (1.0 mg/50 μl) were poured as low and high dose into 6 mm wells on MA and MSA plates formed with sterile cork borer with a micropipette. Ciprofloxacin (0.005 mg/50 μl) and deionized water (50 μl) were designated as positive (+ve) and negative (−ve) controls. Antimicrobial efficacy was assessed by measuring the inhibition zones (in mm) using vernier caliper after incubation of plates at 37 °C for 12 hours. The antimicrobial efficacy of Zr-doped TiO_2 was considered statistically significant using a one-way analysis of variance (ANOVA).[68]

2.6 Molecular docking study

Molecular docking study of Zr-doped TiO_2 nanoparticles was performed to gain insight into molecular interactions at atomic level. Since discovery of trimethoprim and other sulfonamide
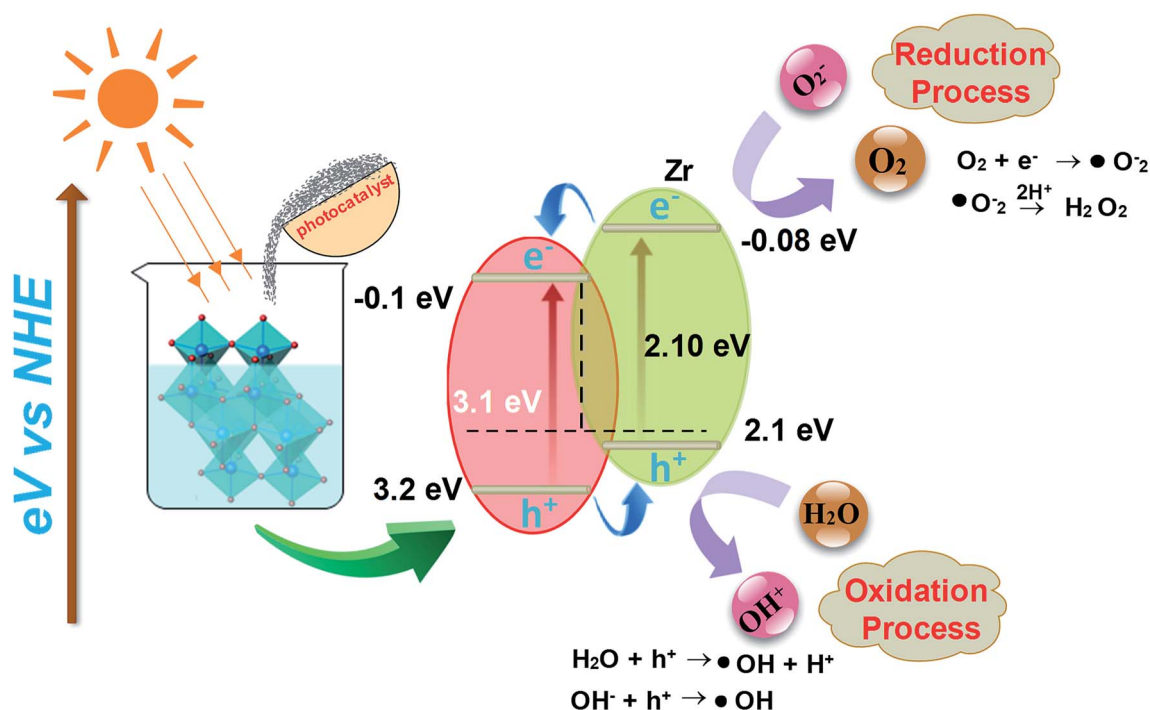

Fig. 2 Photocatalytic mechanism of dye degradation in the presence of Zr–TiO_2 photocatalyst.

drugs, the folate biosynthetic pathway represents an attractive target for new antibiotics discovery.[69,70] Similarly, DNA gyrase is essential for bacterial survival and represents another attractive target for antibiotics discovery.[71,72] Here, we selected dihydrofolate reductase (an approved target of trimethoprim) and dihydropteroate synthase (inhibited by sulfonamide drugs) from folate biosynthetic pathway along with DNA gyrase from both *E. coli* and *S. aureus* as a possible target to explore the binding interaction of Zr-doped TiO_2 nanoparticles with their binding sites.

The target proteins structures were obtained as 3D-crystals from protein data bank with PDB ID: 2ANQ at 2.1 Å Resolution,[73] PDB ID: 5U0V at 1.7 Å resolution,[74] and PDB ID: 6KZX at 2.1 Å resolution,[75] for dihydrofolate reductase (DHFR), dihydropteroate synthase (DHPS) and DNA gyrase, respectively

from *E. coli* as shown in Fig. 3a–c. Similarly, the crystal structures used in case of *S. aureus* possess PDB ID: 3FY8 at 2.2 Å resolution,[76] for dihydrofolate reductase, PDB ID: 4HB7 at 1.9 Å resolution for dihydropteroate synthase and PDB ID: 5CTU at 1.4 Å resolution[77] for DNA gyrase as depicted in Fig. 3d–f.

Molecular docking study of NPs with target proteins was performed using Molecular Operating Environment (MOE) software.[42] Preparation of target protein structures was a multistep process that involved (i) removal of water, (ii) removal of crystallized ligand, (iii) addition of hydrogen atoms, and (iv) energy minimization. The target protein structure was protonated using the 3D-protonation tool of MOE and energy minimization was undertaken using default parameters of energy minimization algorithm (MMFF94x force
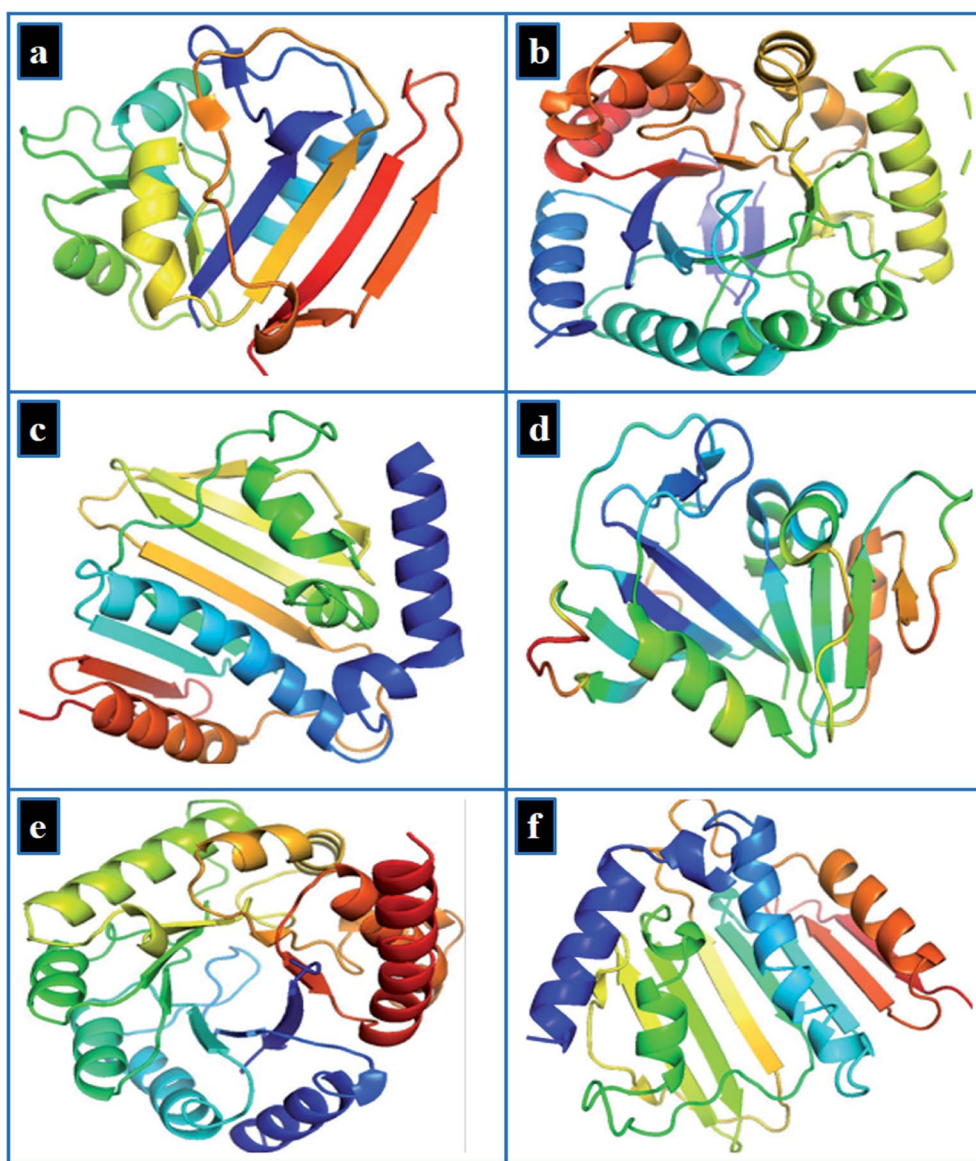

Fig. 3 3D-structure of target proteins of *E. coli*, (a) dihydrofolate reductase (PDB: 2ANQ), (b) dihydropteroate synthase (PDB: 5U0V), (c) DNA gyrase (PDB: 6KZX) and for *S. aureus* (d) dihydrofolate reductase (PDB: 3FY8), (e) dihydropteroate synthase (PDB: 4HB7), (f) DNA gyrase (PDB: 5CTU).
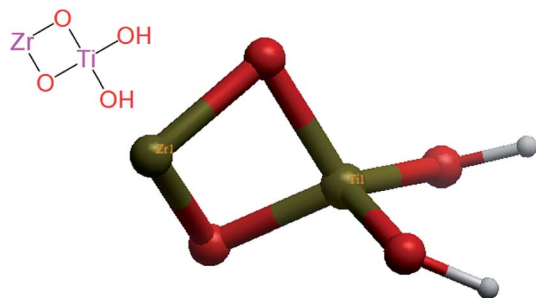
Fig. 4 Structure of Zr-doped TiO_2 nanoparticles.

field, gradient: 0.05) of MOE. Later, systematic conformational search at default parameters (RMS gradient of 0.001 kcal mol^{-1}) using Site Finder was carried out on these protein models. Finally binding pocket of target protein was specified within 10 Å co-crystallized ligand. To get the best binding interaction of Zr-doped TiO_2 nanoparticles inside active pocket, 10 top-ranked docking conformations were generated and the lowest energy conformation was used for further NPs-protein interaction analysis in each case. Both

MOE and DS visualizer[78] were used for the analysis of docking results and representation of their 3D-view.

The crystal structures of anatase TiO_2 in.cif format were obtained from PubChem and modified using Gaussian 09 software to generate Zr-doped TiO_2 NPs structure for docking as shown in Fig. 4.

2.7 Materials characterization

Structural properties and crystallite size were measured using XRD (PAN analytical X'pert pro XRD) with Cu-Kα radiation ($\lambda = 0.154$ nm), diffraction angle varying from 20° to 80°. The presence of functional groups was detected with FTIR using Perki-nElmer spectrometer. FESEM and HR-TEM were employed to study surface morphologies using JEOL JSM-6460LV, and JEM 2100F, respectively coupled with EDS spectrometer. Absorption spectra were acquired using a UV-visible-Genesys 10S spectro-photometer. PL spectroscopy was carried out to study migration and recombination of electron–hole pairs using a spectrofluo-rometer (JASCO, FP-8300). The Molecular Operating Environ-ment (MOE) software was employed for molecular docking study.
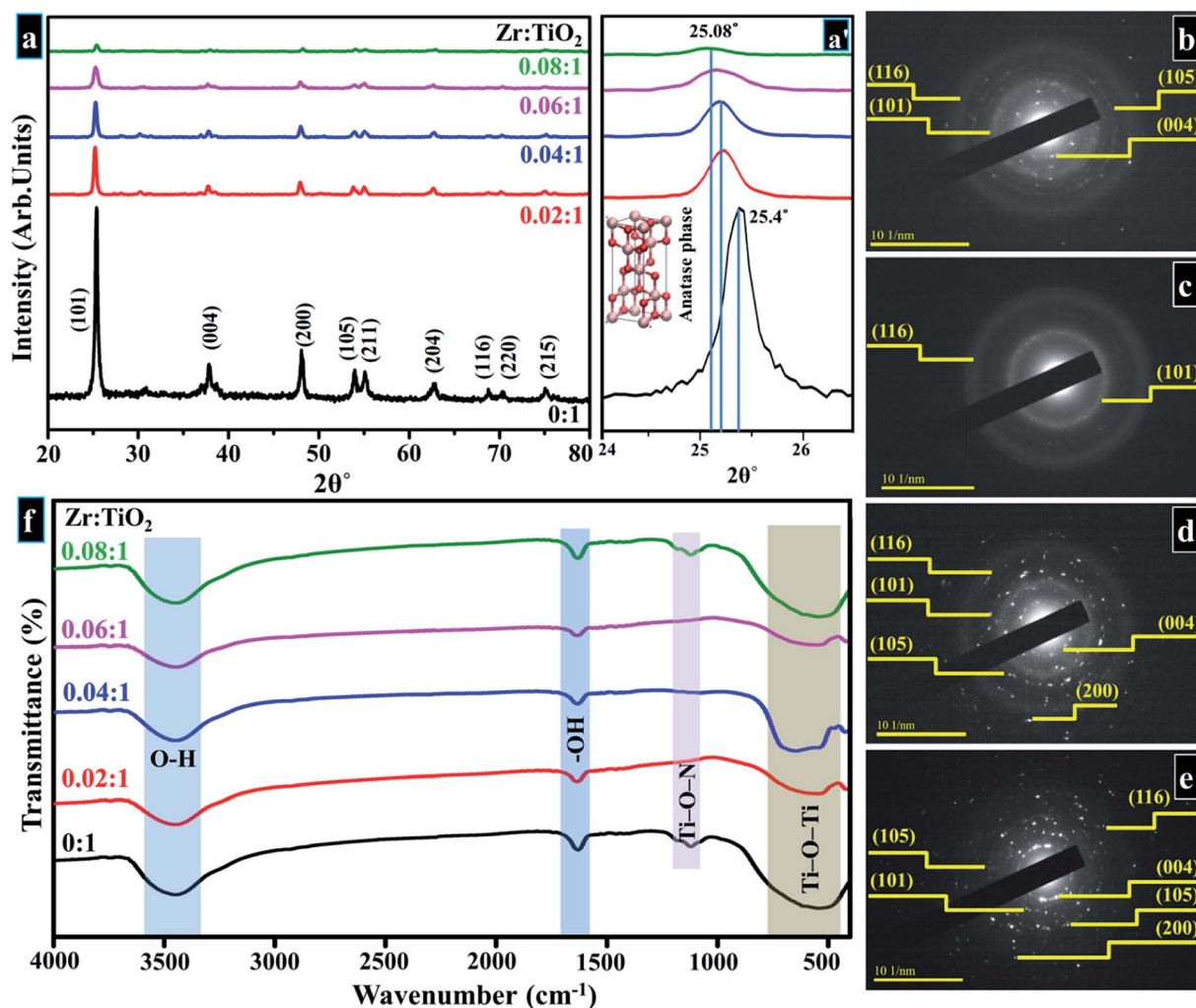

Fig. 5 (a) XRD pattern (a′) zoomed area of (101) plane (b−e) SAED profiles of as-prepared and Zr-doped TiO_2, respectively (f) FTIR spectra.

Table 1 Average crystallite size and E_g values with Zr concentration

Zr : TiO$_2$	Crystallite size (nm)	E_g (eV)
0 : 1	22.22	3.23
0.02 : 1	19.51	2.91
0.04 : 1	18.90	2.53
0.06 : 1	17.26	2.22
0.08 : 1	15.03	2.10

3.   Results and discussion

XRD was employed to analyze crystal structure, phase purity, and crystallite sizes of prepared samples. Diffractogram is plotted between 10–80° as shown in Fig. 5a. In acquired spectra, distinct reflections are located around ~25.47°, 37.79°, 48.18°, 53.87°, 55.17°, 62.68°, 68.74°, 70.29° and 75.05° which are indexed as (101), (004), (200), (105), (211), (204), (116), (220), and (215) planes, respectively. These crystallographic planes correspond to the tetragonal structure of anatase phase of Zr-doped TiO$_2$ associated with standard spectrum (JCPDS card 21-1272) along $I4_1/amd$ (141) space group.[51,79–84] The interlayer spacing was ~0.35 nm for TiO$_2$ corresponding to (101) plane, which was also verified with HR-TEM observation (see Fig. 8). A slight shift to higher values in layer spacing (0.355 nm) upon Zr doping is attributed to homogeneous distribution of dopant elements between interlayers of host sample that is consistent with the peaks shift observed in XRD analysis.[36,85,86]

With Zr incorporation, no obvious peak originating from the dopant or formation of any crystal phase of dopant species was observed in XRD spectra. This observation does not imply the absence of Zr-based plane/phases in the doped samples. It simply suggests that Zr ions are homogenously distributed in TiO$_2$ matrix, and concentration of dopant is too low for detection with XRD.[36,51,79,87] The ionic radius of Zr^{4+} (0.72 Å) is only slightly larger than that of Ti^{4+} (0.65 Å), which favors substitutional doping such that Zr^{4+} dopant ions replace Ti^{4+} ions and occupy their lattice positions within TiO$_2$ matrix. This replacement causes an enlargement in cell volume, such an effect is larger for samples with higher doping concentrations of Zr^{4+} ions incorporated in host lattice. XRD spectra show a linear shift of (101) anatase peak to lower diffraction angles (25.4° to 25.08°) with increasing Zr^{4+} content (Fig. 5a').[51,79,87–91] However, the introduction of large-sized Zr nanoparticles contributes to the development of lattice strain and ultimately causes formation of oxygen sites and prevention of grain growth.[85] The crystallite sizes of samples were calculated by using Debye Scherer formula in eqn 11.

$$D = \frac{0.9\lambda}{\beta \cos\theta} \tag{11}$$

where D is crystallite size, λ is X-ray wavelength (0.154 nm), and β is full width at half maxima (FWHM) of an intense peak (101). Reduction in crystallite size follows the increasing trend in Zr
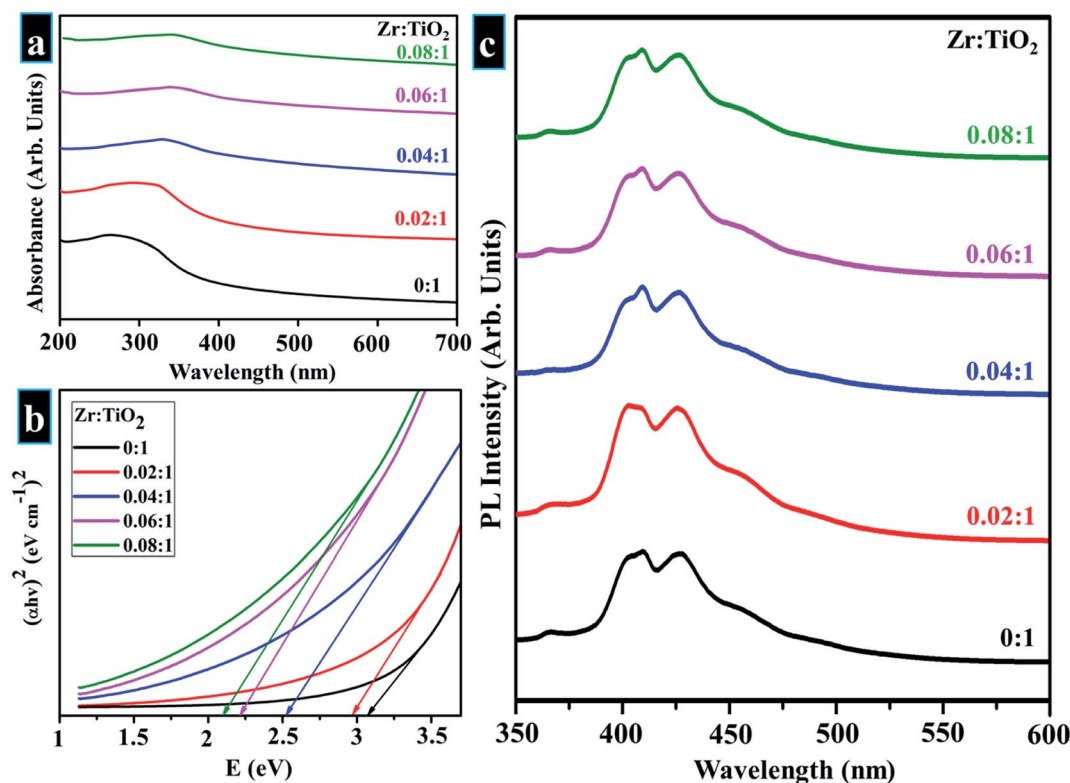

Fig. 6 (a) Absorbance spectra obtained from pure and Zr-doped TiO$_2$ nanoparticles (b) band gap determination (c) PL spectra of prepared samples.

concentration as shown in Table 1.[36,85–87,91,92] SAED analysis of bare and doped samples exhibited distinct rings corresponding to various planes of anatase Zr–TiO$_2$ nanoparticles as shown in Fig. 5b–e. These outcomes are ascribed to well-crystallized specimens, which match well with XRD findings.

FTIR spectra revealed attached functional groups corresponding to their molecular vibration modes as presented in Fig. 5f. An ample absorption band appearing between 400 - 700 cm^{-1} in the acquired spectrum was attributed to the vibration modes of Ti–O–Ti linkage present within TiO$_2$
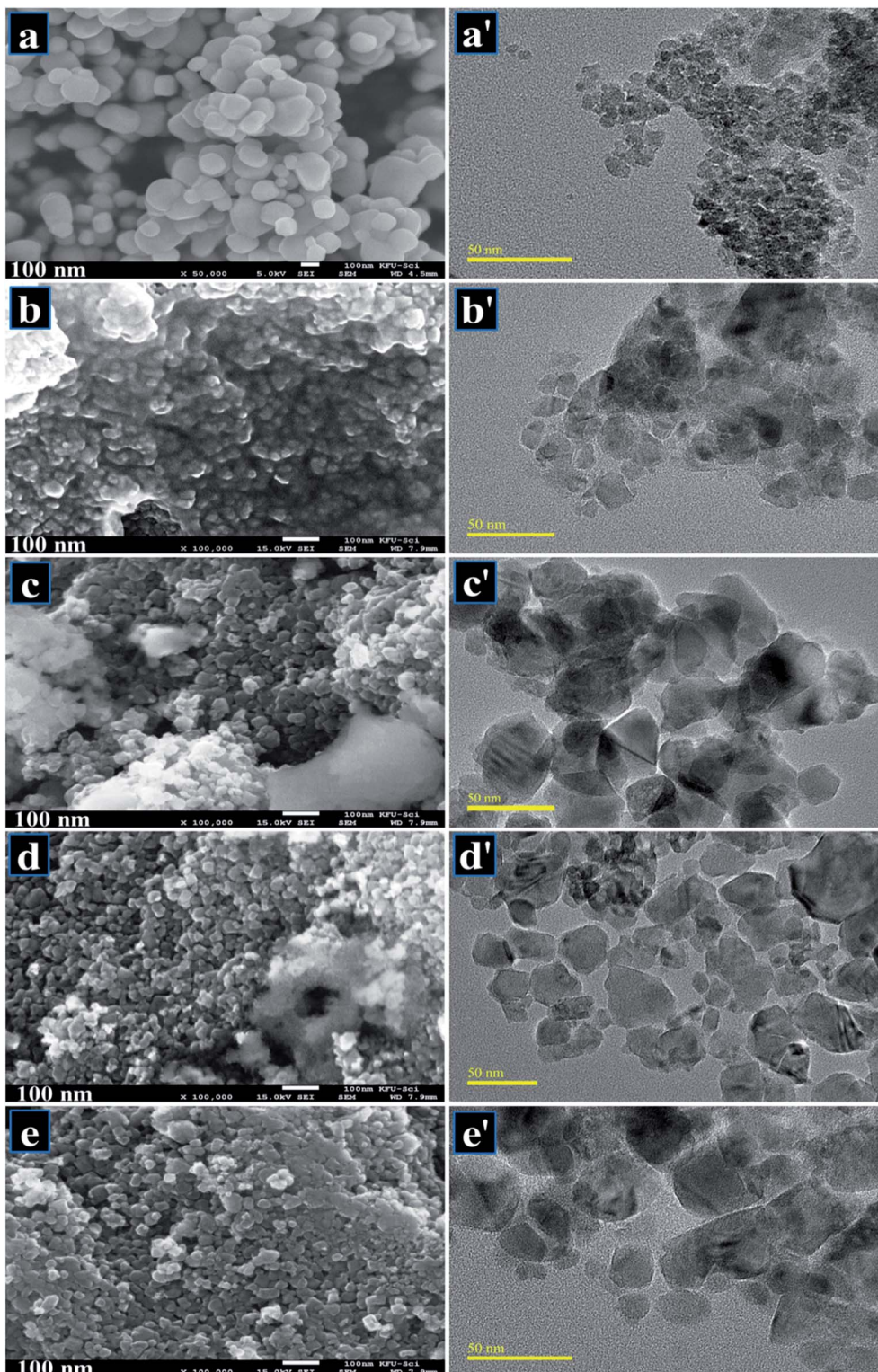

Fig. 7 (a−e) FESEM images of 0 : 1, 0.02 : 1, 0.04 : 1, 0.06 : 1, and 0.08 : 1 samples, respectively (a′−e′) corresponding HR-TEM micrographs of TiO$_2$ and 0 : 02 : 1, 0.04 : 1, 0.06 : 1, and 0.08 : 1 samples, respectively.

nanoparticles, which denotes the formation of TiO_2.[91,93–96] The low absorption band around ~1062 cm^{-1} forms due to Ti–O–N bonding.[97] The measurable band between 3300–3600 cm^{-1} is synonymous with stretching vibrations of O–H and a distinctive band at ~1632 cm^{-1} was ascribed to bending vibrations of hydroxyl ions (–OH).[91,93,94,98] This vibration band is related to the protons of physisorbed water in prepared samples.[99,100] According to reported literature, titanium oxide conserves adsorbed un-dissociated water molecules due to strong Lewis acidity of coordinatively unsaturated Ti^{4+} surface sites.[99]

UV-vis spectroscopy was employed in the study of optical characteristics of prepared samples as seen in spectra displayed in Fig. 6a (200–700 nm). The aim was to examine optimum absorption of ultraviolet-visible light as well as to measure band gap according to band shifting. Optical electronic excitations to a conductive band from the absorptive band are generally characterized by enrichment of absorptive band with a certain wavelength in acquired absorption spectrum.[99] Pristine TiO_2 shows a continuous upsurge in optical absorption at a lower wavelength with maximum broad absorption range appearing in UV zone at 300 nm.[91,93,101–103] Doped samples revealed a slight shift in optical absorption edge towards longer wavelength (visible region) with increasing Zr content as well as a difference in average crystallite size that leads to variations in band gap values of doped samples as depicted in Fig. 6b.[58,87,91,94] Band gap energies were estimated by using the Tauc equation as labeled in eqn (12).

$$\alpha h\nu = K(h\nu - E_g)^n \tag{12}$$

where α is absorption coefficient, h denotes Planck's constant, ν is frequency and K is absorption index. The value of exponent (n) is associated with the electronic nature of band gap and corresponds to direct allowed transitions (1/2), indirect allowed transitions (2), direct forbidden transitions (3/2), and indirect forbidden transitions (3).[104,105] Even though band gap of Zr is around 5.0 eV, due to its strong similarity in its isovalent state with Ti^{4+} such that electronegativity of Zr^{4+} (1.40) is comparable with that of Ti^{4+} (1.54), absorption edge shifts to visible region with a presumable reduction in band gap (see Table 1) caused by either defects produced by trace concentration of Zr^{4+} in TiO_2 lattice or by reduced crystal domains.[58,92,94,106] An obvious change in optical absorbance of nanomaterials as a function of crystallite size may occur due to quantum confinement effects.[91] This variation in optical properties (redshift in wavelength) is considered a primary prerequisite for the enhancement of photocatalytic behavior of nanoparticles.[94]

PL spectroscopy was employed to perceive excitons (electron–hole pairs) recombination rate under action of light, while acquired spectra are displayed in Fig. 6c. The excitation wavelength of all samples is $\lambda_{max} = 380$ nm, and emission peak was observed at ~415 nm, which reveals direct transition (band–band) and phonon-assisted indirect transition (via. band-gap state) of anatase TiO_2.[107] Rate of recombination by photogenerated charge is reduced due to surface defects. Metal ions and oxygen opening separately trap excited electron and hole. The excited electron moves from valance band to new state present due to doping, therefore it serves to decrease PL intensity.[108] For all samples, PL spectra were unaffected by doping.

FESEM was employed to investigate surface morphology of pure and doped samples. Micrograph of host TiO_2 as shown in Fig. 7a indicates agglomeration of TiO_2 with spherical
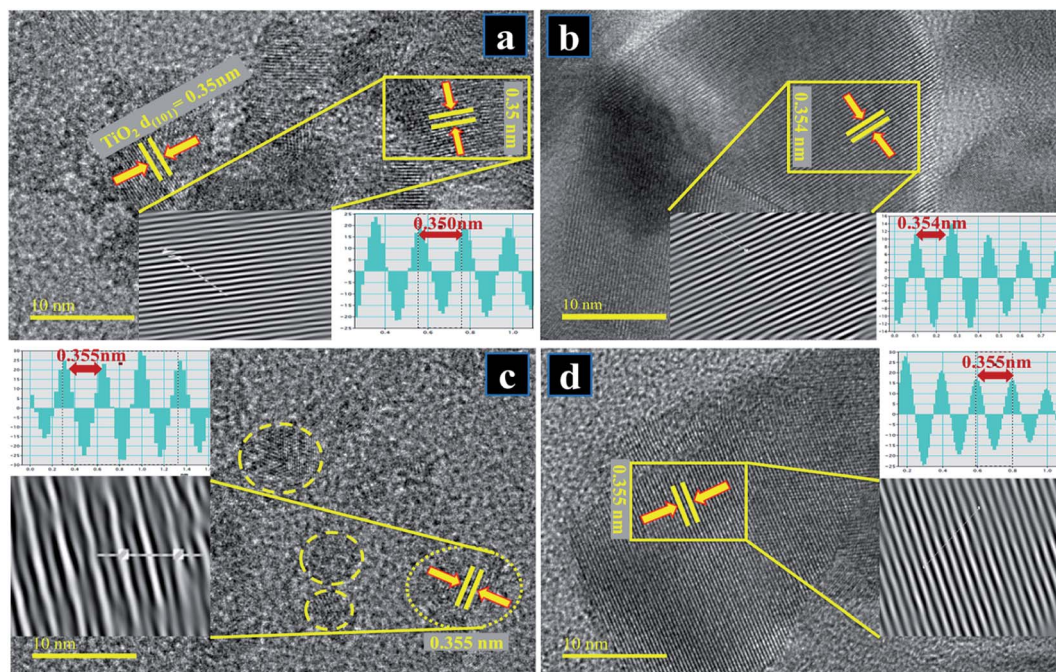

Fig. 8 HR-TEM images up to 10 nm resolution used for measuring interlayer spacing of samples for (a) pure TiO_2 (b) 0.02 : 1 (c) 0.04 : 1 (d) 0.06 : 1.
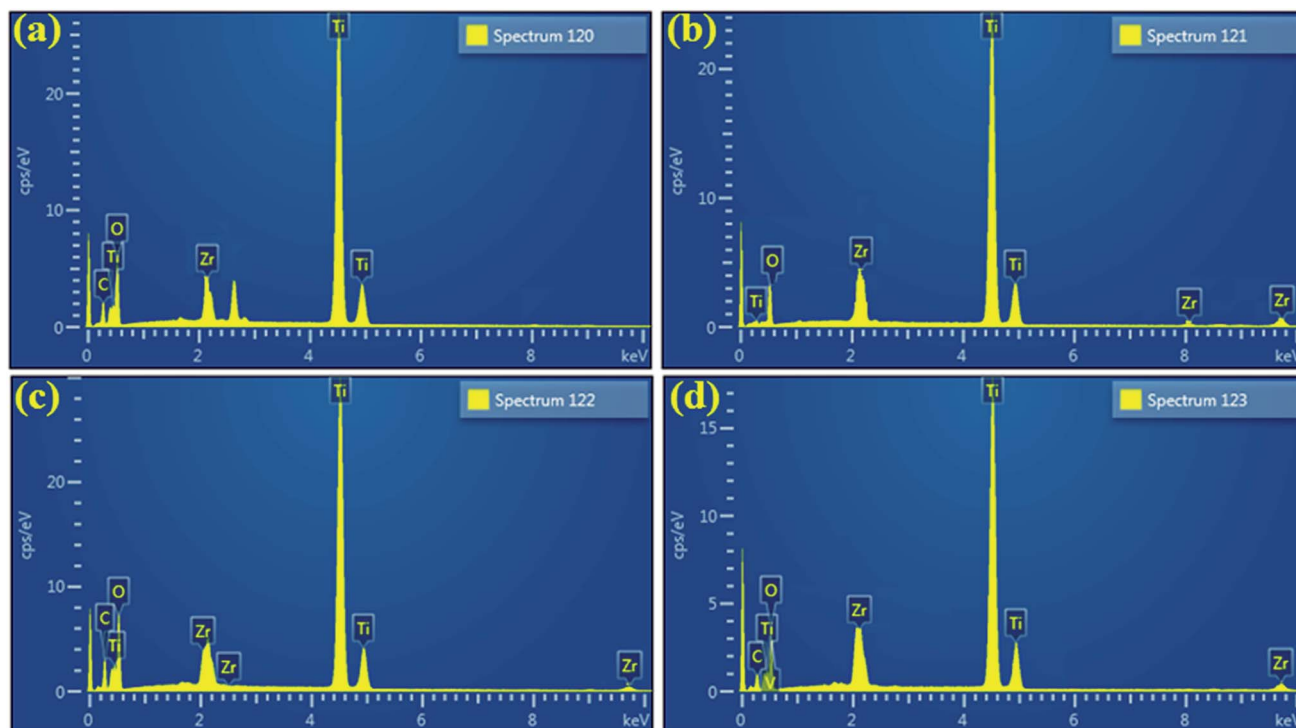
Fig. 9 (a–d) EDS profiles of prepared samples (a) 0 : 1 (b) 0.02 : 1 (c) 0.04 : 1 (d) 0.08 : 1.

morphology. Fig. 7b–e also indicate spherical shape with an average particle size of ~20 nm. Agglomeration arises due to the instability of TiO_2 nanoparticles, which leads them to join together until they stabilize. The growth of nanoparticles was homogeneous and aggregation of nanoparticles was observed on the surface. It is noteworthy that large-sized finite aggregates were observed, which suggests that aggregation had occurred throughout the washing stage while the calcined temperature used during synthesis was relatively high. HR-TEM images revealed further information about the morphology of particles as depicted in Fig. 7a′–e′. Pure sample shows highly agglomerated nanoparticles with spherical morphology (Fig. 7a′). Upon

doping with Zr, particles get scattered to some extent with random distribution observed in Fig. 7b′ and c′. With increasing concentration of dopant, agglomeration was observed to decrease along with slight transparency of nanoparticles (Fig. 7d′). Sample doped with the highest Zr concentration (Fig. 7e′) showed random disruption of stony particles and chunk areas with highly agglomeration trend.

HR-TEM microscopy at a higher resolution (up to 10 nm) was employed to seek detailed information about morphology and interlayer spacing. HR-TEM micrographs presented in Fig. 8a–d on a single grain show distinct atomic planes well-ordered in O–Ti–O arrangement to form a single layer and periodic atomic
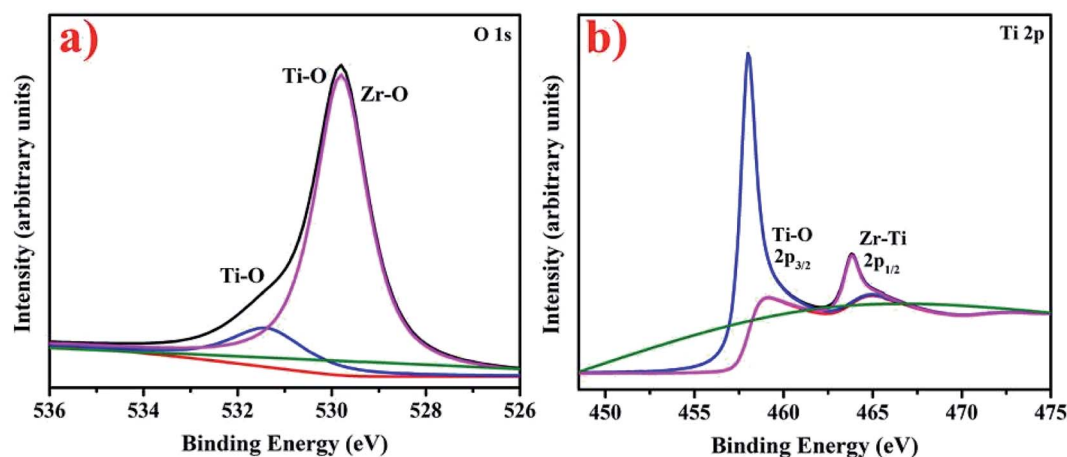

Fig. 10 (a and b) XPS spectra of Zr : TiO_2 (0.08 : 1) (a) O 1s (b) Ti 2p.
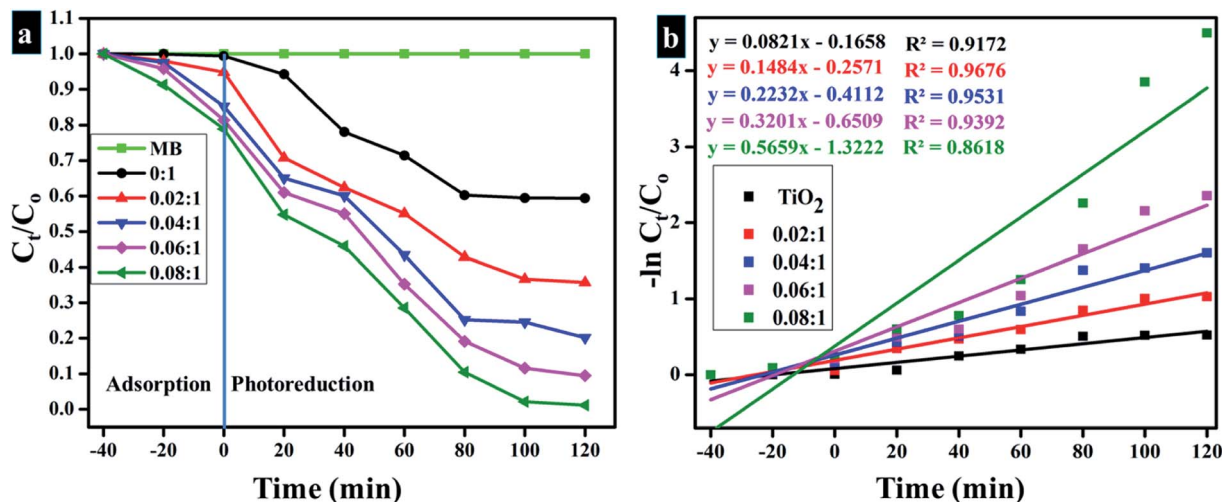
Fig. 11 (a) Plot of concentration ratio (C_t/C_0) *versus* time (b) Plot of $-\ln(C_t/C_0)$ *versus* time spectra for dye reduction.

arrangement at particular areas, where interplanar spacing was measured to be ~0.350 nm for pure TiO$_2$ (Fig. 8a). According to the periodic arrangement in lattice fringe image, this matches up with (101) facet of anatase TiO$_2$ phase and corresponds well with XRD results.[85,86] In Fig. 8b–d with the addition of dopant, d-spacing of Zr–TiO$_2$ nanoparticles was slightly enlarged and found to be ~0.354–0.355 nm which is consistent with the peak shifts observed in XRD spectra (see Fig. 5a′).[86]

EDS was employed to evaluate the elemental composition with an aim to verify the purity of samples. According to EDS profiles illustrated in Fig. 9b–d, strong peaks of Ti element at 4.50 (Ti K$_\alpha$) and 4.96 keV (Ti K$_\beta$), oxygen peak at 0.52 keV (O K$_\alpha$), and Zr peak at 2.04 keV (Zr L$_\alpha$) along with various other positions were detected, which confirms the formation of pure anatase TiO$_2$ as well as suggests the successful incorporation of dopant species. Moreover, carbon peak appearing below 1 keV is caused by carbon tabs that are utilized to hold sample during SEM analysis or/and due to background counts in SEM-EDS detector.

XPS analysis elucidating the chemical composition of synthesized nanostructures and presenting O 1s and Ti 2p

spectra of synthesized Zr–TiO$_2$ nanostructures is shown in Fig. 10a and b. According to the literature, pure TiO depicts two peaks in O 1s spectra at 530.0 eV and 531.8 eV corresponding to Ti–O and O–H links in TiO$_2$, respectively.[109] The peak positioned at 531.8 eV in O 1s spectra corresponds to Ti–O and similarly, peak positioned at 529.8 eV ascribes to Ti–O and Zr–O in Fig. 10a.[110] The Ti 2p high-resolution XPS spectra consist of two peaks at 458.5 and 464.8 eV, which correspond to Ti–O and Zr–Ti, respectively in Fig. 10b.[110] These are present in addition of pure TiO$_2$ peaks at 458.6 eV (2p$_{3/2}$) and 464.4 eV (2p$_{1/2}$) indicating existence of Ti in +4 oxidation state.[111] The presented 2p$_{3/2}$ and 2p$_{1/2}$ peaks in Ti 2p spectra in Fig. 10b depicts redshift related to pure TiO$_2$ peaks as per literature[111] thus, the resulting decrease in binding energy confirms successful Zr doping in TiO$_2$.[111]

Fig. 11a and b labels parameters shown by the light-induced activity of Zr-doped TiO$_2$ nanoparticles. According to these outcomes, absorbance is presented as time-dependent function. Fig. 11a reveals photocatalytic response of nanoparticles and clearly shows that MB degradation gradually increases with increasing concentration of the dopant. Substantial

Table 2 Comparative study of prepared sample with previously published data

|	Literature			Present study					
	Synthesis	Phase	Max. degradation		Sample	Synthesis	Phase	Max. degradation and rate constants (min^{-1})		
Zr–TiO$_2$ NPs	[8]Sol–gel	Anatase	50%	90 min	0 : 1	Sol–gel	Anatase	40%	0.0042	120 min
	[13]Mechanical ball milling	Anatase	90%	120 min						
	[15]Sol–gel	Anatase	82%	180 min	0.02 : 1			65%	0.0085	
	[51]Sol–gel	Anatase	98%	120 min	0.04 : 1			80%	0.0131	
	[86]Sol–gel	Anatase	75%	150 min						
	[87]Sol–gel	Anatase	80%	60 min						
	[91]Acid modified sol–gel	Anatase	62%	80 min	0.06 : 1			96%	0.0191	
	[64]Sol–gel	Anatase	99%	120 min	0.08 : 1			99%	0.0373	
	[115]Sol–gel	Anatase	85%	350 min						
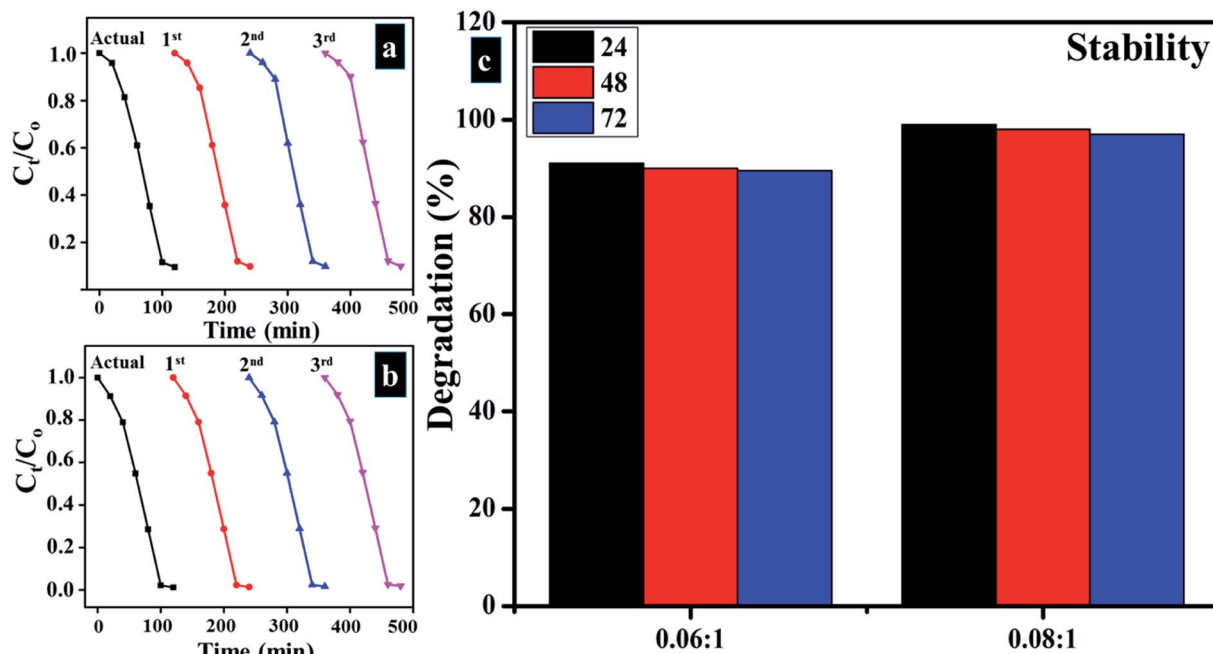
Fig. 12 (a and b) Plots of C_t/C_o vs. time for reusability of 0.06 : 1, and 0.08 : 1, samples respectively (c) stability of Zr-doped samples (0.06 : 1, and 0.08 : 1).

degradation is shown by the sample doped with the highest concentration of Zr (0.08 : 1), which was up to 99% in 120 minutes. Lesser extent of degradation was shown by samples in

dark whereas in the presence of light, samples showed considerable removal of MB within 120 minutes. Only 40% degradation occurred in case of pure TiO_2, however with Zr
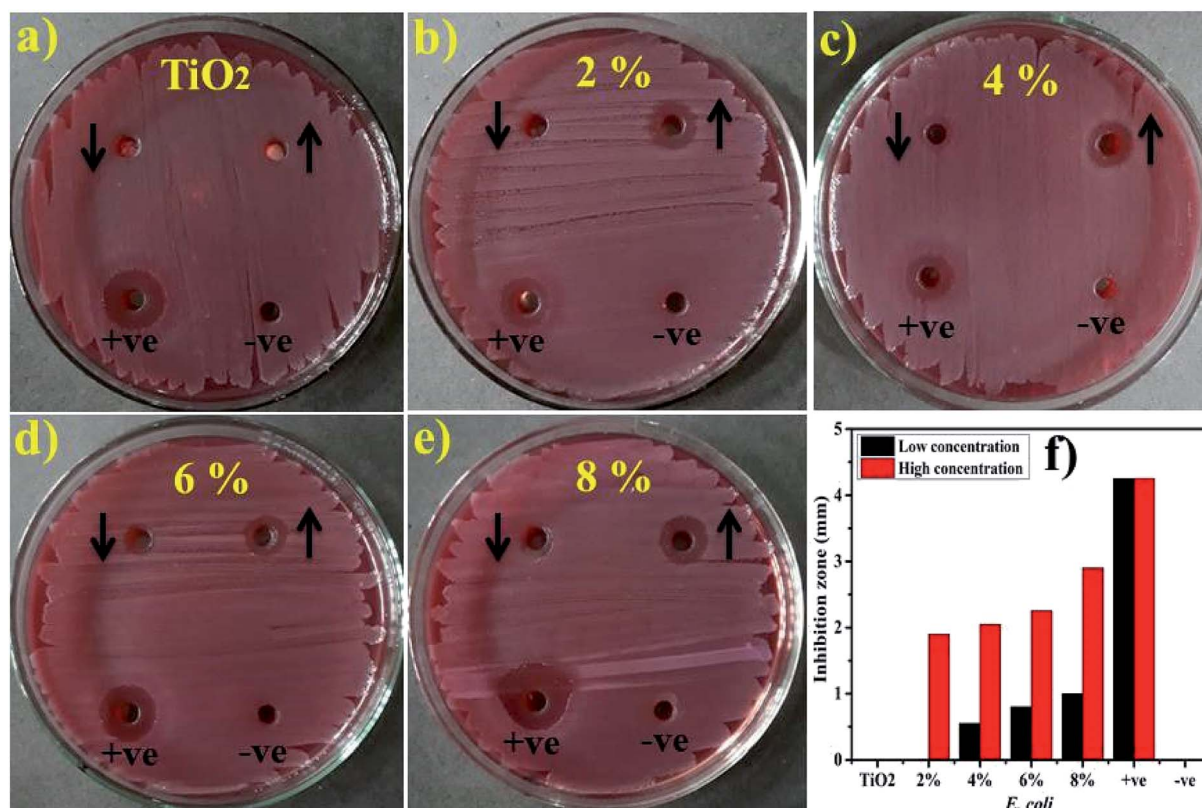

Fig. 13 (a) In vitro antimicrobial efficacy of TiO_2 (control), (b) 2% Zr-doped (c) 4%-doped, (d) 6%-doped, (e) 8%-doped against E. coli (f) graphical presentation.
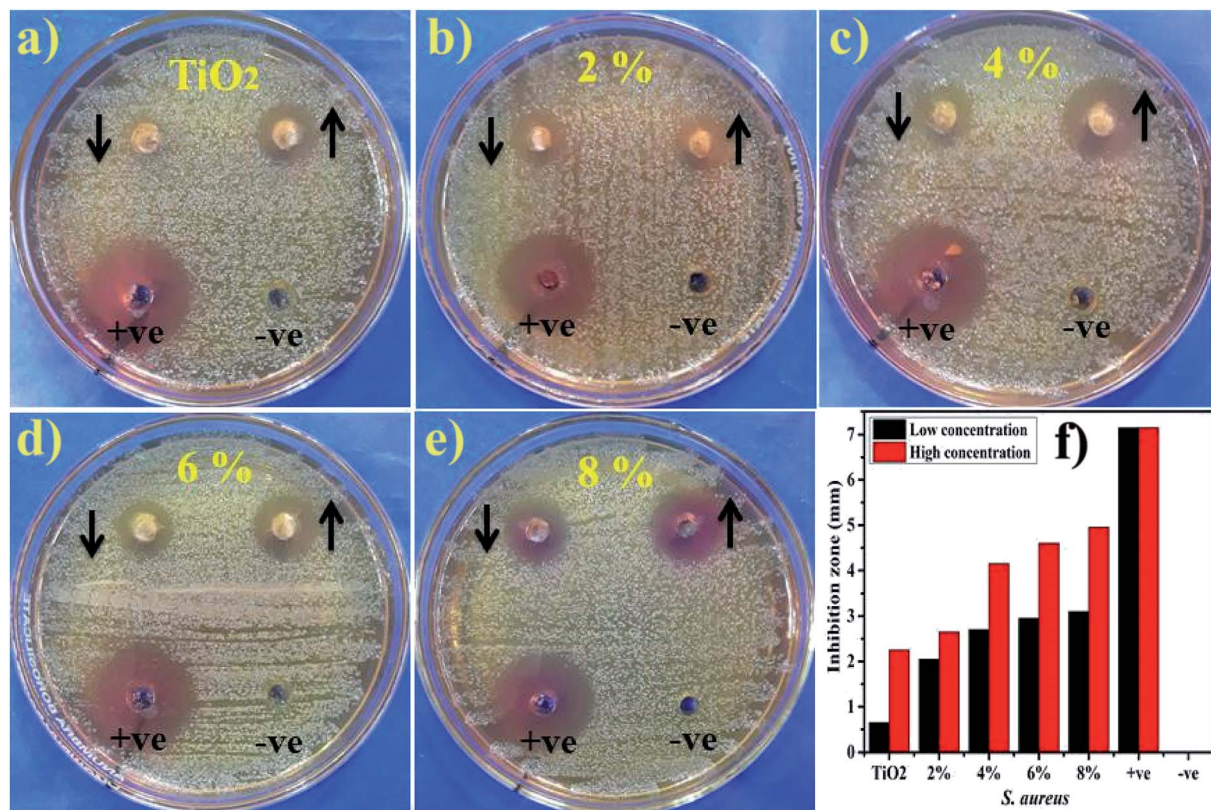
Fig. 14 (a) *In vitro* antimicrobial efficacy of TiO$_2$ (control), (b) Zr-doped TiO$_2$ (2%), (c) (4%), (d) (6%), (e) (8%) against *S. aureus* (f) graphical presentation.

doping, photocatalysts showed remarkable degradation since Zr reduces band gap and inhibits recombination rate. The understanding of photo-degradation kinetics by rate constants (k) that was calculated by measuring slopes on $\ln(C_t/C_o)$ curves are drawn against time, as revealed in Fig. 11b. Rate constants of all samples were calculated by using pseudo-first-order kinetic theory (eqn (13)):

$$-\ln(C_t/C_o) = kt \qquad (13)$$

Rate constant (k) increase with an increase in doping ratio (Table 2).[27,112–114] As discussed above, the enhanced photocatalytic activity of nanoparticles may be ascribed mainly to these measures: firstly, the preservation of structure in nanoparticles as well as a high specific surface area that promotes broad absorption of UV irradiation within the catalyst and provides more surface active sites for reactants, thus helping to enhance the activities of photo-degradation. Secondly, the incorporation of Zr in TiO$_2$ lattice inhibits the growth of anatase crystal during annealing, thus the resulting smaller anatase crystals provide photo-induced electron–hole pairs with shorter migration periods therefore assisting in wider availability of reaction sites, which ultimately results in the improvement of photocatalytic performance. Thirdly, Zr^{4+} insertion could clearly prevent the loss of surface hydroxyl related groups on nanoparticles, thereby effectively trapping photo-induced holes in preserved surface hydroxyl groups and thus creating active

hydroxyl radicals with high oxidant efficiency. More decisively, the electron–hole recombination may be prevented efficiently by the establishment of hydroxyl groups and appropriate oxygen sites, subsequently, contributing to the enhancement of photocatalytic activity of nanoparticles.[79]

3.1 PH value

Outcome of a photocatalytic experiment greatly depends on pH value as the rate of reaction has been found to possess a direct correlation with pH value. Cited literature reveals that dye

Table 3 Bactericidal action of Zr-doped TiO$_2$

Sample	Inhibition zone^a (mm)		Inhibition zone^b (mm)	
	0.5 mg/50 μl	1.0 mg/50 μl	0.5 mg/50 μl	1.0 mg/50 μl
TiO$_2$	0	0	0.65	2.25
Zr–TiO$_2$ 2%	0	1.9	2.05	2.65
Zr–TiO$_2$ 4%	0.55	2.05	2.7	4.15
Zr–TiO$_2$ 6%	0.8	2.25	2.95	4.6
Zr–TiO$_2$ 8%	1	2.9	3.1	4.95
Ciprofloxacin	4.25	4.25	7.15	7.15
DIW	0	0	0	0

^{a} Inhibition zone (mm) of Zr-doped TiO$_2$ for *E. coli*. ^{b} Inhibition zone measurements of Zr-doped TiO$_2$ for *S. aureus*.

degradation due to photocatalytic activity yields superior results under alkaline or basic conditions. In the current study, pH value was measured which corresponds to basic alkaline condition of the performed experiment. The outcomes of this work demonstrating efficient dye degradation under alkaline conditions favorably support experimental results and reported literature[25,32,60]

3.2 Reusability

Reusability of catalysts is considered a significant factor as photocatalyst should be reusable in order to utilize it up to the maximum number of cycles for treatment of industrial wastewater. Reusability was determined for the sample as of stability up to three cycles. The obtained results are presented in Fig. 12a and b which indicates that Zr-doped TiO$_2$ catalyst can be utilized as an effective reusable photocatalyst.

3.3 Stability

Stability of experimental results was determined by allowing the accomplished activities to be retained for three days. Every 24 hours, absorption spectra were obtained from the samples to note any variation in dye degradation potential. Stability of catalysts is illustrated in Fig. 12c by means of percentage degradation which specifies obtained product as highly stable photocatalyst for dye degradation as no reduction in results was
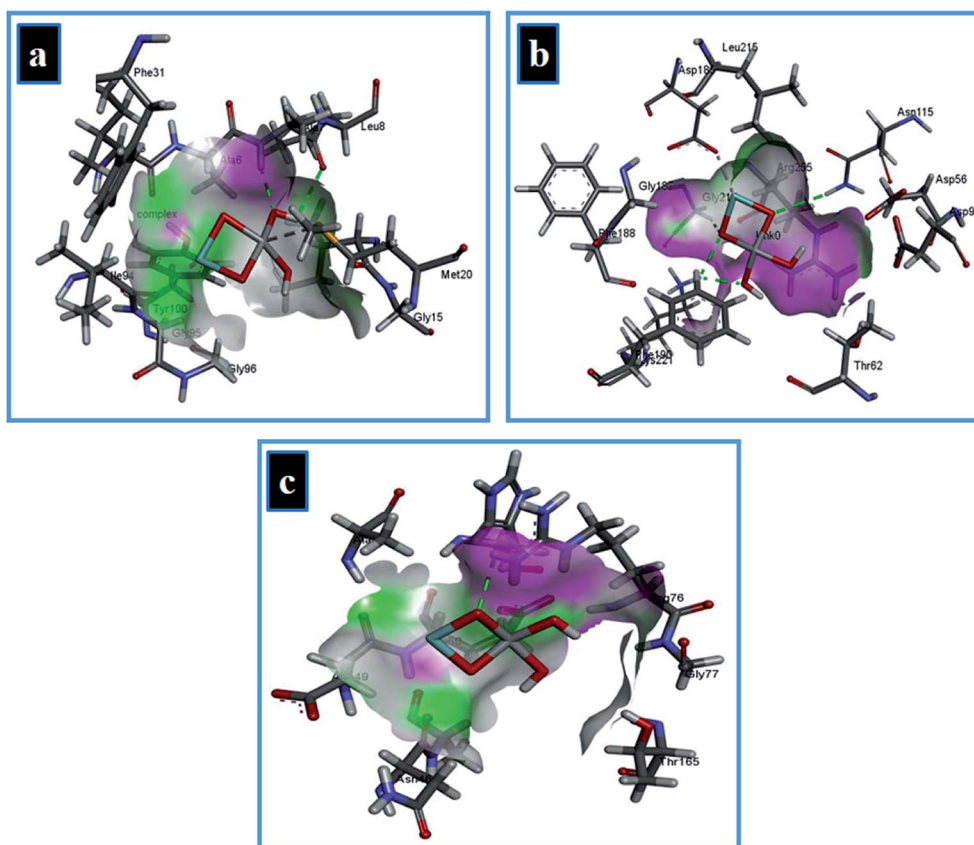
detected after 96 hours of stopover. As catalysts doped with higher Zr concentrations exhibited superior results, therefore, it was considered sufficient to determine the stability of (0.06 : 1, and 0.08 : 1) samples only.

3.4 Load of catalyst

Lastly, the load of catalyst before performing catalytic and photocatalytic activity and after four cycles of reusability was assessed. The load of catalyst before performing photocatalytic activity was 10 mg, after four times of recycling it was detected as 9.6 mg by allowing 5% sensing/detecting deviation.

The *in vitro* antimicrobial potential of Zr-doped TiO$_2$ against G −ve and G +ve isolated from caprine mastitic milk with graphical presentations are shown in Fig. 13, and 14 and summarized in Table 3. The results depict enhanced bactericidal action and synergism of Zr-doped TiO$_2$ against *S. aureus* compared with *E. coli* Fig. 13a–f. Statistically significant ($P <$ 0.05) inhibition zones were recorded as (0.65–3.1 mm) and (2.25–4.95 mm) against *S. aureus* (Fig. 14a–f) while, (0–1 mm) and (0–2.9 mm) against *E. coli* at low and high doses, respectively. TiO$_2$ control showed null efficacy against *E. coli* at a low and high dose. The % age efficacy increased from (28.6–43.3%) to (37.0–69.2%) against *S. aureus* and similarly, from (0–23.5%) to (44.7–68.2%) against *E. coli*. Ciprofloxacin as positive control inhibited (7.15 mm) and (4.25 mm) *S. aureus* and *E. coli* growth, respectively compared with DIW (0 mm). Overall, Zr-doped TiO$_2$

Fig. 15 Binding interaction pattern of Zr-doped TiO$_2$ nanoparticles with active site residues of (a) dihydrofolate reductase, (b) dihydropteroate synthase, and (c) DNA gyrase from *E. coli*.

material resulted in significant ($P < 0.05$) bactericidal efficacy against G +ve compared with G –ve.

The oxidative stress produced by nanoparticles directly depends on concentration, shape and size of nanoparticles. Antimicrobial activity in terms of inhibition zones (mm) increased due to higher wt% doping of Zr with maximum cations availability. Antimicrobial effectiveness depends primarily on concentration and size, which exhibits inverse relation to the size of doped material.[60,67,68] Small-sized NPs generate more reactive oxygen species (ROS) which stay effective in implants of bacterial membrane resulting in cytoplasmic-contents extrusion and killing bacteria.[116] Secondly, the strong cationic interaction of Zr^{+4} with bacterial membrane negative parts results in enhanced bactericidal activity at increasing concentrations by inducing cell lysis and collapse of bacteria.[24,117]

Molecular docking study was undertaken to understand the possible molecular interactions responsible for antibacterial activity of Zr-doped TiO$_2$ nanoparticles against *E. coli* and *S. aureus*. Folate biosynthetic pathway leads to synthesis of tetra-hydrofolate that plays an essential role in the biosynthesis of various bioactive constituents namely thymidylate enzyme, pantothenic acid, nitrogenous bases such as purine, ribonucleic acid and amino acids. Enzymes belonging to this pathway *e.g.*, dihydrofolate reductase and dihydropteroate synthase have been reported as attractive targets for antibiotic discovery. Trimethoprim is a well-known antibiotic target DHFR while DHPS is inhibited by sulfonamide class of antibiotics.[70,118] Keeping in view the importance and essentiality of folate biosynthetic pathway for growth and survival of bacteria, binding interaction pattern of these nanoparticles were evaluated against DHFR, DHPS and DNA gyrase enzyme from both *E. coli* and *S. aureus*.

In case of DHFR from *E. coli*, the Zr-doped TiO$_2$ nanoparticle showed H-bonding interaction with Ala7 and Ile14 while Ile94 interacted through metal contact with a binding score of -9.87 kcal mol^{-1} as shown in Fig. 15a. Similarly, for DHPS from *E. coli*, the best binding score observed was -9.14 kcal mol^{-1} possessing H-bonding interaction with Lys221 and Asp115 along with metal contact interaction with Asp185. In addition, the binding score -4.31 kcal mol^{-1} in case of DNA gyrase is attributed to H-bonding interaction with Arg76 of active site along with metal contact interaction with Glu50 as depicted in Fig. 15b and c.

The best-docked conformation of Zr-doped TiO$_2$ nanoparticles against DHFR enzyme from *S. aureus* has -11.32 kcal mol^{-1} binding score and involve H-bonding interaction with Ala7 and Leu5 while Asp27 of active site formed metal contact interaction as shown in Fig. 16a. In case of DHPS from *S. aureus*, NPs revealed metal contact interaction with Glu142 and Asn134 along with H-bonding interaction with Asn130 of active pocket with overall binding score of -7.61 kcal mol^{-1} (Fig. 16b).

The Zr-doped TiO$_2$ nanoparticles interacted with Thr173, Asp81 through H-bonding interaction and metal contact with
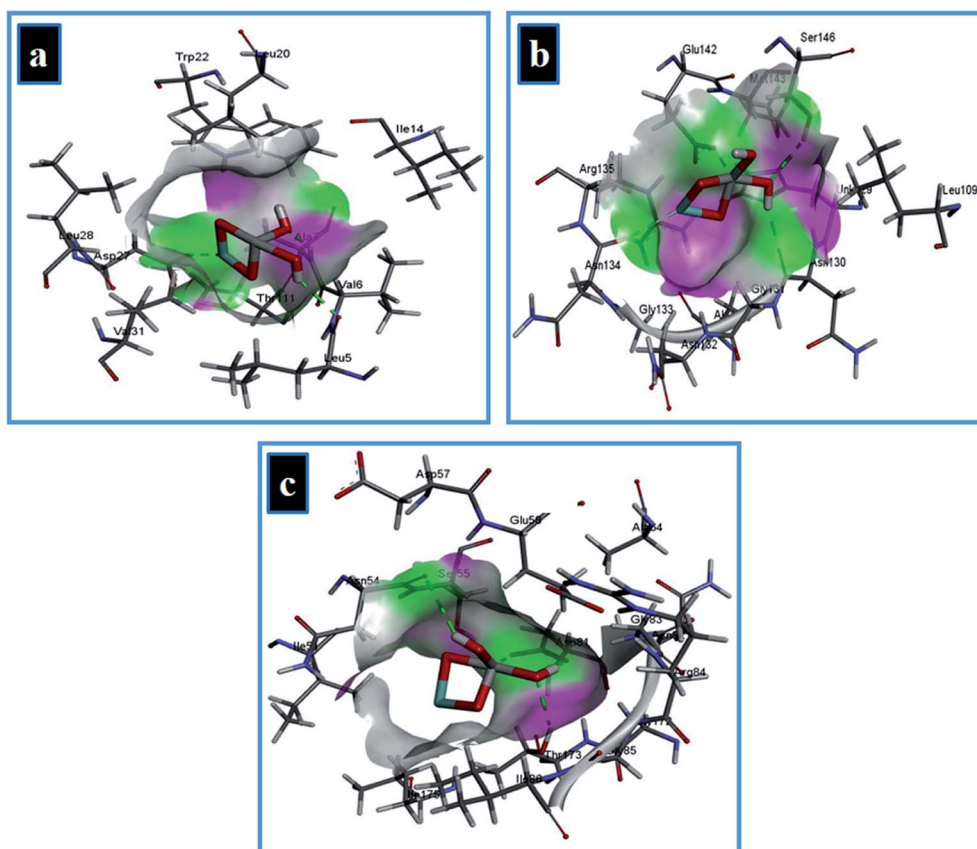

Fig. 16 Binding interaction pattern of Zr-doped TiO$_2$ nanoparticles with active site residues of (a) dihydrofolate reductase, (b) dihydropteroate synthase, (c) DNA gyrase from *S. aureus*.

Ser55 of binding pocket of DNA gyrase from *S. aureus* (binding score -8.33 kcal mol^{-1}) as depicted in Fig. 16c. *In silico* findings suggested Zr-doped TiO$_2$ nanoparticles as a possible inhibitor of enzymes from folate biosynthetic pathway and DNA gyrase and their enzyme inhibition studies are recommended for further analysis.

4. Conclusion

Zr-doped TiO$_2$ was successfully synthesized *via* sol–gel chemical method and prepared samples were analyzed through various characterization techniques. XRD profiles showed the formation of anatase phase with a slight shift in (101) facet towards lower angle suggesting the presence of a dopant that is well dispersed in TiO$_2$ crystal. Crystallite size was reduced (from 22.22 to 15.03 nm) upon incorporation of Zr. All functional groups observed were related to the samples and characteristic absorption band between 400–900 cm^{-1} was ascribed to the vibration modes of Ti–O–Ti linkage in TiO$_2$ nanoparticles that indicate the formation of pure TiO$_2$ as illustrated with FTIR. The spectrum obtained using UV-vis unveiled an absorption tail that trailed towards visible region (redshift) with increasing concentrations of dopant that caused the band gap to narrow (from 3.23 to 2.10 eV). Spherical morphology of nanoparticles exhibiting a high degree of agglomeration was visualized through SEM and HR-TEM with a *d*-spacing of ~0.350 nm measured for pure sample and ~0.353 nm for sample doped with the highest concentration. EDS data showed elemental composition that revealed successful doping of Zr. In addition, Zr-doped TiO$_2$ depicted enhanced bactericidal action and synergism against *S. aureus* compared with *E. coli* isolated from caprine mastitis thus, opening new gateway for use of doped nanomaterials as potential bactericidal agents. The findings of molecular docking study suggested Zr-doped TiO$_2$ as potential inhibitor against dihydrofolate reductase, dihydropteroate synthase and DNA gyrase enzyme as possible targets. *In silico* findings are in good agreement with observed bactericidal activity against *E. coli* and *S. aureus*. Photocatalytic activity corresponding to Zr–TiO$_2$ (0.08 : 1) degraded 99% of MB concentration. These results obtained from prepared nanocatalysts show no hazardous behavior in wastewater treatment and point toward an excellent nanocatalyst that is stable, reusable and more importantly can be employed for elimination of organic pollutants from wastewater.

Conflicts of interest

There are no conflicts to declare.

Acknowledgements

References

1 A. Wypych, I. Bobowska, M. Tracz, A. Opasinska, S. Kadlubowski, A. Krzywania-Kaliszewska, J. Grobelny and P. Wojciechowski, *J. Nanomater.*, 2014, **2014**, 124814.

2 R. Abazari, A. R. Mahjoub and S. Sanati, *RSC Adv.*, 2014, **4**, 56406–56414.

3 Y. Cui, L. Zhang, K. Lv, G. Zhou and Z.-S. Wang, *J. Mater. Chem. A*, 2015, **3**, 4477–4483.

4 V. R. Desai, S. M. Hunagund, M. S. Pujar, M. Basanagouda, J. S. Kadadevarmath and A. H. Sidarai, *J. Mol. Liq.*, 2017, **233**, 166–172.

5 N. Lagopati, E. P. Tsilibary, P. Falaras, P. Papazafiri, E. A. Pavlatou, E. Kotsopoulou and P. Kitsiou, *Int. J. Nanomed.*, 2014, **9**, 3219–3230.

6 R. Kumar, R. El-Shishtawy and M. Barakat, *Catalysts*, 2016, **6**, 76.

7 M. Ikram, E. Umar, A. Raza, A. Haider, S. Naz, A. Ul-Hamid, J. Haider, I. Shahzadi, J. Hassan and S. Ali, *RSC Adv.*, 2020, **10**, 24215–24233.

8 D. Kapusuz, J. Park and A. Ozturk, *J. Phys. Chem. Solids*, 2013, **74**, 1026–1031.

9 Z. G. Shang, Z. Q. Liu, P. J. Shang and J. K. Shang, *J. Mater. Sci. Technol.*, 2012, **28**, 385–390.

10 S. S. R. Putluru, L. Schill, A. D. Jensen, B. Siret, F. Tabaries and R. Fehrmann, *Appl. Catal., B*, 2015, **165**, 628–635.

11 H. Sun, C. Wang, S. Pang, X. Li, Y. Tao, H. Tang and M. Liu, *J. Non-Cryst. Solids*, 2008, **354**, 1440–1443.

12 A. R. Dalod, L. Henriksen, T. Grande and M. A. Einarsrud, *Beilstein J. Nanotechnol.*, 2017, **8**, 304–312.

13 T. Tokmakci, A. Ozturk and J. Park, *Ceram. Int.*, 2013, **39**, 5893–5899.

14 N. B. Shali and S. Sugunan, *J. Sol-Gel Sci. Technol.*, 2007, **42**, 101–105.

15 N. N. Binitha, Z. Yaakob and R. Resmi, *Cent. Eur. J. Chem.*, 2010, **8**, 182–187.

16 J. Moma and J. Baloyi, in *Photocatalysts-Applications and Attributes*, IntechOpen, 2018.

17 K. Nakata and A. Fujishima, *J. Photochem. Photobiol., C*, 2012, **13**, 169–189.

18 A. Fujishima, X. Zhang and D. A. Tryk, *Surf. Sci. Rep.*, 2008, **63**, 515–582.

19 J. Schneider, M. Matsuoka, M. Takeuchi, J. Zhang, Y. Horiuchi, M. Anpo and D. W. Bahnemann, *Chem. Rev.*, 2014, **114**, 9919–9986.

20 L. Yang, L. E. Yu and M. B. Ray, *Water Res.*, 2008, **42**, 3480–3488.

21 M. M. Matlock, B. S. Howerton and D. A. Atwood, *Water Res.*, 2002, **36**, 4757–4764.

22 Q. Wen, J. Di, Y. Zhao, Y. Wang, L. Jiang and J. Yu, *Chem. Sci.*, 2013, **4**, 4378–4382.

23 A. Raza, M. Ikram, M. Aqeel, M. Imran, A. Ul-Hamid, K. N. Riaz and S. Ali, *Appl. Nanosci.*, 2019, **10**, 1535–1544.

24 M. Ikram, M. I. Khan, A. Raza, M. Imran, A. Ul-Hamid and S. Ali, *Phys. E*, 2020, **124**, 114246.

25 M. Ikram, J. Hassan, M. Imran, J. Haider, A. Ul-Hamid, I. Shahzadi, M. Ikram, A. Raza, U. Qumar and S. Ali, *Appl. Nanosci.*, 2020, DOI: 10.1007/s13204-020-01439-2.

26 M. Hosseini, N. Fazelian, A. Fakhri, H. Kamyab, K. K. Yadav and S. Chelliapan, *J. Photochem. Photobiol., B*, 2019, **194**, 128–134.

27 M. Ikram, A. Raza, M. Imran, A. Ul-Hamid, A. Shahbaz and S. Ali, *Nanoscale Res. Lett.*, 2020, **15**, 95.

28 M. Ikram, R. Tabassum, U. Qumar, S. Ali, A. Ul-Hamid, A. Haider, A. Raza, M. Imran and S. Ali, *RSC Adv.*, 2020, **10**, 20559–20571.

29 X. Li, Z. Zhang, A. Fakhri, V. K. Gupta and S. Agarwal, *Int. J. Biol. Macromol.*, 2019, **136**, 469–475.

30 A. Raza, U. Qumar, J. Hassan, M. Ikram, A. Ul-Hamid, J. Haider, M. Imran and S. Ali, *Appl. Nanosci.*, 2020, DOI: 10.1007/s13204-020-01475-y.

31 V. S. Mohite, M. S. Mahadik, S. S Kumbhar, Y. M. Hunge, J. H. Kim, A. V. Moholkar, K. Y. Rajpure and C. H. Bhosale, *J. Photochem. Photobiol., B*, 2015, **142**, 204–211.

32 J. Hassan, M. Ikram, A. Ul-Hamid, M. Imran, M. Aqeel and S. Ali, *Nanoscale Res. Lett.*, 2020, **15**, 75.

33 Q. Guo, C. Zhou, Z. Ma and X. Yang, *Adv. Mater.*, 2019, **31**, 1901997.

34 N. Laoufi, D. Tassalit and F. Bentahar, *Global NEST J.*, 2008, **10**, 404–418.

35 N. Bsiri, M. A. Zrir, A. Bardaoui and M. Bouaïcha, *Ceram. Int.*, 2016, **42**, 10599–10607.

36 A. Juma, I. Oja Acik, A. T. Oluwabi, A. Mere, V. Mikli, M. Danilson and M. Krunks, *Appl. Surf. Sci.*, 2016, **387**, 539–545.

37 D.-E. Gu, B.-C. Yang and Y.-D. Hu, *Catal. Commun.*, 2008, **9**, 1472–1476.

38 Y. Ohko, I. Ando, C. Niwa, T. Tatsuma, T. Yamamura, T. Nakashima, Y. Kubota and A. Fujishima, *Environ. Sci. Technol.*, 2001, **35**, 2365–2368.

39 A. Fakhri, V. K. Gupta, H. Rabizadeh, S. Agarwal, N. Sadeghi and S. Tahami, *Int. J. Biol. Macromol.*, 2018, **120**, 1789–1793.

40 Q. Huang, W. Ma, X. Yan, Y. Chen, S. Zhu and S. Shen, *J. Mol. Catal. A: Chem.*, 2013, **366**, 261–265.

41 B. Duan, Y. Zhou, C. Huang, Q. Huang, Y. Chen, H. Xu and S. Shen, *Ind. Eng. Chem. Res.*, 2018, **57**, 14044–14051.

42 T. W. Shattuck, *Colby College Molecular Mechanics Exercises MOE (Molecular Operating Environment), Exercises*, 2011, http://www.colby.edu/chemistry/CompChem/MOEtutor09.pdf.

43 D. Das, H. K. Mishra, K. M. Parida and A. K. Dalai, *J. Mol. Catal. A: Chem.*, 2002, **189**, 271–282.

44 J. Lukáč, M. Klementová, P. Bezdička, S. Bakardjieva, J. Šubrt, L. Szatmáry, Z. Bastl and J. Jirkovský, *Appl. Catal., B*, 2007, **74**, 83–91.

45 Ş. Ţălu, S. Stach, M. Ikram, D. Pathak, T. Wagner and J.-M. Nunzi, *Int. J. Nanosci.*, 2014, **13**, 1450020.

46 B. Moongraksathum, J.-Y. Shang and Y.-W. Chen, *Catalysts*, 2018, **8**, 352.

47 N. Perkas, A. Lipovsky, G. Amirian, Y. Nitzan and A. Gedanken, *J. Mater. Chem. B*, 2013, **1**, 5309–5316.

48 A. M. Alotaibi, B. A. D. Williamson, S. Sathasivam, A. Kafizas, M. Alqahtani, C. Sotelo-Vazquez, J. Buckeridge, J. Wu, S. P. Nair, D. O. Scanlon and I. P. Parkin, *ACS Appl. Mater. Interfaces*, 2020, **12**, 15348–15361.

49 S. S. Surah, S. Sirohi, R. Nain and G. Kumar, *AIP Conf. Proc.*, 2018, **1932**, 030038.

50 M. A. Ashraf, Y. Yang and A. Fakhri, *Ceram. Int.*, 2020, **46**, 8379–8384.

51 M. C. Sekhar, B. Purusottam Reddy, K. Mallikarjuna, G. Shanmugam, C.-H. Ahn and S.-H. Park, *Mater. Res. Express*, 2018, **5**, 015024.

52 A. Kubacka, M. S. Diez, D. Rojo, R. Bargiela, S. Ciordia, I. Zapico, J. P. Albar, C. Barbas, V. A. Martins dos Santos, M. Fernandez-Garcia and M. Ferrer, *Sci. Rep.*, 2014, **4**, 4134.

53 A. Manafi Khajeh Pasha, M. Hosseini, A. Fakhri, V. K. Gupta and S. Agarwal, *J. Mol. Liq.*, 2019, **289**, 110950.

54 R. D. Desiati, M. Taspika and E. Sugiarti, *Mater. Res. Express*, 2019, **6**, 095059.

55 C. L. de Dicastillo, M. G. Correa, F. B. Martínez, C. Streitt and M. J. Galotto, in *Titanium Dioxide*, IntechOpen, 2020.

56 U. Joost, K. Juganson, M. Visnapuu, M. Mortimer, A. Kahru, E. Nõmmiste, U. Joost, V. Kisand and A. Ivask, *J. Photochem. Photobiol., B*, 2015, **142**, 178–185.

57 M. Khan, M. R. Shaik, S. T. Khan, S. F. Adil, M. Kuniyil, M. Khan, A. A. Al-Warthan, M. R. H. Siddiqui and M. Nawaz Tahir, *ACS Omega*, 2020, **5**, 1987–1996.

58 D. Campoccia, S. Ravaioli, R. Vivani, A. Donnadio, E. Vischini, A. Russo, L. Visai, C. R. Arciola, L. Montanaro and M. Nocchetti, *Materials*, 2019, **12**, 3184.

59 X. Wang, D. Chen, L. Cao, Y. Li, B. J. Boyd and R. A. Caruso, *ACS Appl. Mater. Interfaces*, 2013, **5**, 10926–10932.

60 U. Qumar, M. Ikram, M. Imran, A. Haider, A. Ul-Hamid, J. Haider, K. N. Riaz and S. Ali, *Dalton Trans.*, 2020, **49**, 5362–5377.

61 M. Ikram, S. Ali, R. Murray, A. Hussain, d. Islah u and S. I. Shah, *Curr. Appl. Phys.*, 2015, **15**, 48–54.

62 S. Altaf, H. Ajaz, M. Imran, A. Ul-Hamid, M. Naz, M. Aqeel, A. Shahzadi, A. Shahbaz and M. Ikram, *Appl. Nanosci.*, 2020, DOI: 10.1007/s13204-020-01350-w.

63 A. Wahab, M. Imran, M. Ikram, M. Naz, M. Aqeel, A. Rafiq, H. Majeed and S. Ali, *Appl. Nanosci.*, 2019, **9**, 1823–1832.

64 B. Gao, T. M. Lim, D. P. Subagio and T.-T. Lim, *Appl. Catal., A*, 2010, **375**, 107–115.

65 A. Ajmal, I. Majeed, R. N. Malik, H. Idriss and M. A. Nadeem, *RSC Adv.*, 2014, **4**, 37003–37026.

66 A. Gnanaprakasam, V. M. Sivakumar and M. Thirumarimurugan, *Indian Journal of Materials Science*, 2015, **2015**, 1–16.

67 A. Haider, M. Ijaz, M. Imran, M. Naz, H. Majeed, J. A. Khan, M. M. Ali and M. Ikram, *Appl. Nanosci.*, 2020, **10**, 1095–1104.

68 A. Haider, M. Ijaz, S. Ali, J. Haider, M. Imran, H. Majeed, I. Shahzadi, M. M. Ali, J. A. Khan and M. Ikram, *Nanoscale Res. Lett.*, 2020, **15**, 50.

69 M. V. B. Dias, J. C. Santos, G. A. Libreros-Zúñiga, J. A. Ribeiro and S. M. Chavez-Pacheco, *Future Med. Chem.*, 2018, **10**, 935–959.

70 S. Hawser, S. Lociuro and K. Islam, *Biochem. Pharmacol.*, 2006, **71**, 941–948.

71 A. Maxwell, *Trends Microbiol.*, 1997, **5**, 102–109.

72 L. L. Silver, *Cold Spring Harbor Perspect. Med.*, 2016, **6**, a030239.

73 R. L. Summerfield, D. M. Daigle, S. Mayer, D. Mallik, D. W. Hughes, S. G. Jackson, M. Sulek, M. G. Organ, E. D. Brown and M. S. Junop, *J. Med. Chem.*, 2006, **49**, 6977–6986.

74 M. L. Dennis, M. D. Lee, J. R. Harjani, M. Ahmed, A. J. DeBono, N. P. Pitcher, Z.-C. Wang, S. Chhabra, N. Barlow, R. Rahmani, B. Cleary, O. Dolezal, M. Hattarki, L. Aurelio, J. Shonberg, B. Graham, T. S. Peat, J. B. Baell and J. D. Swarbrick, *Chem.–Eur. J.*, 2018, **24**, 1922–1930.

75 F. Ushiyama, H. Amada, T. Takeuchi, N. Tanaka-Yamamoto, H. Kanazawa, K. Nakano, M. Mima, A. Masuko, I. Takata, K. Hitaka, K. Iwamoto, H. Sugiyama and N. Ohtake, *ACS Omega*, 2020, **5**, 10145–10159.

76 C. Oefner, S. Parisi, H. Schulz, S. Lociuro and G. E. Dale, *Acta Crystallogr., Sect. D: Biol. Crystallogr.*, 2009, **65**, 751–757.

77 M. F. Mesleh, J. B. Cross, J. Zhang, J. Kahmann, O. A. Andersen, J. Barker, R. K. Cheng, B. Felicetti, M. Wood, A. T. Hadfield, C. Scheich, T. I. Moy, Q. Yang, J. Shotwell, K. Nguyen, B. Lippa, R. Dolle and M. D Ryan, *Bioorg. Med. Chem. Lett.*, 2016, **26**, 1314–1318.

78 BIOvIA, D. S., *Discovery studio modeling environment*, Dassault Systemes, San Diego, Release, 4, 2015.

79 J. Song, X. Wang, J. Yan, J. Yu, G. Sun and B. Ding, *Sci. Rep.*, 2017, **7**, 1636.

80 T. Aguilar, J. Navas, R. Alcántara, C. Fernández-Lorenzo, J. J. Gallardo, G. Blanco and J. Martín-Calleja, *Chem. Phys. Lett.*, 2013, **571**, 49–53.

81 X. Wei, G. Zhu, J. Fang and J. Chen, *Int. J. Photoenergy*, 2013, **2013**, 1–6.

82 K. Thamaphat, P. Limsuwan and B. J. K. J. Ngotawornchai, *Kasetsart Journal - Natural Science*, 2008, **42**, 357–361.

83 S. Watanabe, X. Ma and C. Song, *J. Phys. Chem. C*, 2009, **113**, 14249–14257.

84 S. P. Suriyaraj and R. Selvakumar, *RSC Adv.*, 2014, **4**, 39619–39624.

85 I. Singh and B. I. Birajdar, in *Titanium Dioxide, Material for a Sustainable Environment*, 2018, ch. 5, DOI: 10.5772/intechopen.74568.

86 I. Singh, R. Kumar and B. I. Birajdar, *J. Environ. Chem. Eng.*, 2017, **5**, 2955–2963.

87 R. Schiller, C. K. Weiss and K. Landfester, *Nanotechnology*, 2010, **21**, 405603.

88 J. Lukáč, M. Klementová, P. Bezdička, S. Bakardjieva, J. Šubrt, L. Szatmáry and A. Grusková, *J. Mater. Sci.*, 2007, **42**, 9421–9428.

89 M. Krunks, A. Mere, I. Oja Acik, A. O. Juma and A. T. Oluwabi, *Proc. Est. Acad. Sci.*, 2018, **67**, 147–157.

90 J. Wang, Y. Yu, S. Li, L. Guo, E. Wang and Y. Cao, *J. Phys. Chem. C*, 2013, **117**, 27120–27126.

91 P. Goswami and J. N. Ganguli, *Dalton Trans.*, 2013, **42**, 14480–14490.

92 A. P. Larios, J. L. Rico, L. M. A. Esparza, O. A. G. Vargas, N. G. Silva and R. Gómez, *Catalysts*, 2019, **9**, 938.

93 K. V. Bineesh, D. K. Kim and D. W. Park, *Nanoscale*, 2010, **2**, 1222–1228.

94 T. V. L. Thejaswini, D. Prabhakaran and M. A. Maheswari, *J. Photochem. Photobiol., A*, 2017, **344**, 212–222.

95 H. Sezen, M. Buchholz, A. Nefedov, C. Natzeck, S. Heissler, C. Di Valentin and C. Woll, *Sci. Rep.*, 2014, **4**, 3808.

96 G. Mishra and M. Mukhopadhyay, *Sci. Rep.*, 2019, **9**, 4345.

97 B. Rajamannan, S. Mugundan, G. Viruthagiri, P. Praveen and N. Shanmugam, *Spectrochim. Acta, Part A*, 2014, **118**, 651–656.

98 Z. Topalian, G. A. Niklasson, C. G. Granqvist and L. Osterlund, *ACS Appl. Mater. Interfaces*, 2012, **4**, 672–679.

99 R. J. Alvaro, N. D. Diana and A. M. Maria, *Contemp. Eng. Sci.*, 2017, **10**, 1539–1549.

100 Z. A. Ansari, A. Umar, H. Fouad and S. G. Ansari, *J. Nanoelectron. Optoelectron.*, 2015, **10**, 290–294.

101 X. Wang, R. L. Patel and X. Liang, *RSC Adv.*, 2018, **8**, 25829–25834.

102 S.-W. Kim, R. Khan, T.-J. Kim and W. J. Kim, *Bull. Korean Chem. Soc.*, 2008, **29**, 1217–1223.

103 M. Ahamed, M. A. Khan, M. J. Akhtar, H. A. Alhadlaq and A. Alshamsan, *Sci. Rep.*, 2016, **6**, 30196.

104 S. K. Suram, P. F. Newhouse and J. M. Gregoire, *ACS Comb. Sci.*, 2016, **18**, 673–681.

105 B. D. Viezbicke, S. Patel, B. E. Davis and D. P. Birnie, *Phys. Status Solidi B*, 2015, **252**, 1700–1710.

106 C. Gionco, M. C. Paganini, E. Giamello, O. Sacco, V. Vaiano and D. Sannino, *J. Energy Chem.*, 2017, **26**, 270–276.

107 Y. Chen, Y. Wang, W. Li, Q. Yang, Q. Hou, L. Wei, L. Liu, F. Huang and M. Ju, *Appl. Catal., B*, 2017, **210**, 352–367.

108 H. Tang, H. Berger, P. E. Schmid, F. Lévy and G. Burri, *Solid State Commun.*, 1993, **87**, 847–850.

109 G. W. Simmons and B. C. Beard, *J. Phys. Chem.*, 1987, **91**, 1143–1148.

110 H. Chen, G. Jiang, T. Jiang, L. Li, Y. Liu, Q. Huang and W. Chen, *MRS Commun.*, 2015, **5**, 525–531.

111 P. Victor and S. B. Krupanidhi, *J. Phys. D: Appl. Phys.*, 2004, **38**, 41–50.

112 Z. Yao, H. Sun, H. Sui and X. Liu, *Nanoscale Res. Lett.*, 2020, **15**, 78.

113 M. Aqeel, M. Ikram, A. Asghar, A. Haider, A. Ul-Hamid, M. Naz, M. Imran and S. Ali, *Appl. Nanosci.*, 2020, **10**, 2045–2055.

114 M. Ikram, I. Jahan, A. Haider, J. Hassan, A. Ul-Hamid, M. Imran, J. Haider, A. Shahzadi, A. Shahbaz and S. Ali, *Appl. Nanosci.*, 2020, 1–11, DOI: 10.1007/s13204-020-01412-z.

115 C. Belver, J. Bedia and J. J. Rodriguez, *J. Hazard. Mater.*, 2017, **322**, 233–242.

116 W. Fang, X. Chaofa, J. Zheng, G. Chen and K. Jiang, *RSC Adv.*, 2015, **5**, 39612–39619.

117 M. Ikram, S. Abbasi, A. Haider, S. Naz, A. Ul-Hamid, M. Imran, J. Haider and A. Ghaffar, *Nanotechnology*, 2020, **31**, 275704.

118 G. H. Hitchings and J. J. Burchall, *Adv. Enzymol. Relat. Areas Mol. Biol.*, 1965, **27**, 417–468.